NASA Technical Memorandum 78620

Developments in the Computation of Turbulent Boundary Layers

Morris W. Rubesin

September 1979

NASA
National Aeronautics and
Space Administration

NASA Technical Memorandum 78620

Developments in the Computation of Turbulent Boundary Layers

Morris W. Rubesin, Ames Research Center, Moffett Field, California

National Aeronautics and
Space Administration

Ames Research Center
Moffett Field, California 94035

DEVELOPMENTS IN THE COMPUTATION OF TURBULENT BOUNDARY LAYERS

Morris W. Rubesin
Ames Research Center, NASA, Moffett Field, California 94035, U.S.A.

SUMMARY

Computational techniques applicable to turbulent boundary layers are classified into solutions of Reynolds-averaged equations, in which all the effects of the turbulence are modelled, and solutions of three-dimensional, time-dependent Navier-Stokes equations, in which the large eddies are calculated and only the turbulence at scales smaller than the computational mesh spacings has to be modelled. Current computation costs place engineering computations in the first of these categories; large eddy simulations are appropriate currently for special studies of the dynamical processes of turbulence in idealized flow fields. It is shown that the two methods are interrelated and that each can gain from advances in the other. The degree of success of a pair of increasingly complex Reynolds stress models to broaden their range of applicability is examined through comparisons with experimental data for a variety of flow conditions. An example of a large-eddy simulation is presented, compared with experimental results, and used to evaluate the models for pressure rate-of-strain correlations and dissipation in the Reynolds-averaged equations.

NOMENCLATURE

a	transverse body radius
C_1	modelling coefficient in pressure rate-of-strain correlation, turbulence-turbulence interaction (Rotta term)
C_f	skin-friction coefficient
D_{ij}	turbulence production tensor, Eq. (37)
ϵ	turbulence kinetic energy
h	static enthalpy
h''	fluctuating enthalpy in mass-weighted variables
ℓ	length scale
ℓ_m	mixing length
P_{ij}	turbulence production tensor, Eq. (37)
Pr_L	Prandtl number for molecular motions
P^*	mean specific static pressure
p	static pressure
p^*	specific static pressure, p/ρ
$\tilde{p}^*$	resolvable fluctuating specific static pressure
$p^{*'}$	subgrid fluctuating specific static pressure
Q_j	heat flux vector
q	turbulence speed
Re	modelling coefficient, near-wall modification, Eq. (31)
Re_T	turbulence Reynolds number, Eq. (32)
R_ω	modelling coefficient, near wall modification, Eq. (31)
S_{ij}	rate of strain tensor
U_i	mean velocity component in ith direction
u_i	velocity component in the ith direction, mass-weighted in compressible flows
$\tilde{u}_i$	resolvable fluctuating velocity component in ith direction
u_i'	subgrid fluctuating velocity component in ith direction
u''	fluctuating velocity in mass-weighted variables
v_w	surface mass-transfer normal velocity
v'	fluctuating velocity normal to surface
y	distance normal to surface
α	scaling factor in turbulence simulation
$\hat{\alpha}$	modelling coefficient in pressure rate of strain correlation turbulence mean-flow interaction
β	modelling coefficient, Eq. (31), or scaling factor in turbulence simulation
β^*	modelling coefficient, Eq. (31)
$\hat{\beta}$	modelling coefficient in pressure rate of strain correlation – turbulence mean-flow interaction
γ	modelling coefficient, Eq. (31)
γ^*	modelling coefficient, Eq. (31)
$\hat{\gamma}$	modelling coefficient in pressure rate of strain correlation – turbulence mean-flow interaction
δ	boundary-layer thickness
δ_{ij}	Kronecker delta
ϵ	eddy viscosity (turbulence kinematic viscosity)
ϵ	turbulence kinetic energy dissipation rate
ϵ_{ij}	dissipation rates of Reynolds stress component τ_{ij}
ι	boundary-layer edge turbulence intensity factor
λ	low Reynolds number modelling coefficient, Eq. (31)
μ	fluid viscosity
ν	fluid kinematic viscosity
ν_{eff}	effective eddy viscosity in subgrid model
ρ	fluid density
$\tilde{\rho}$	instantaneous fluid density
σ	modelling coefficient, Eq. (31)

σ^*	modelling coefficient, Eq. (31)
τ_{ij}	Reynolds stress component
Ω_{ij}	vorticity tensor
ω	turbulence specific dissipation rate

Subscripts:

e	boundary-layer edge condition or experimental value
w	surface quantity
1,2,3	Cartesian axes direction
$( )_{,i}$	a partial derivative with respect to the ith coordinate

Superscripts:

T	total quantity, turbulent plus molecular process
$(\dot{})$	partial derivative with respect to time

Other:

$< >$	filtered average
$(\bar{})$	time averaged

INTRODUCTION

Advances in computer technology and numerical analysis during the past decade have made it possible to compute the characteristics of turbulent flow fields with a degree of detail that was impossible in the past. This computational power has been applied to problems both in engineering and in basic fluid mechanics. Engineering methods have been confined largely to the solution of statistical equations of turbulence, usually for steady-state conditions. The increased computational power has permitted the use of second-order closure methods wherein partial differential equations are used to describe the scales, intensity, and even the individual components of Reynolds stresses distributed throughout the flow field. It is becoming quite standard in advanced engineering problems to use two-equation models representing the transport of turbulence kinetic energy and a measure of the turbulence scale to establish the local eddy viscosity. The underlying impetus to this work has been the premise that the increased complexity of a model tends to broaden its range of applicability, thereby making it a predictive tool. The past simple models of statistical turbulence, such as the mixing-length models, largely were used to explain flow-field behavior after the experimental results were obtained; they could be used only to interpolate between or moderately extrapolate conditions of a particular experiment. New situations required new experiments to guide modelling changes. With the more detailed second-order closure models, however, the rather large number of experimental coefficients employed requires drawing upon experiments of different kinds of flow fields for evaluating the modelling coefficients of the different mechanisms. For example, the coefficient for the dissipation of turbulence kinetic energy is determined in part from experiments dealing with the decay of isotropic turbulence. Coefficients for terms representing the exchange between individual components of Reynolds stress by the correlation of fluctuations in pressure and the instantaneous rate of strain come largely from experiments in homogeneous turbulence created by either uniform shearing or normal strains. Thus, when these models are used in boundary-layer flows, many of their terms reflect the behavior of turbulence under other conditions, thereby possibly broadening the model's range of applicability. On the other hand, this reliance on a group of different kinds of experiments to establish the modelling coefficients often results in a somewhat less accurate representation of a particular flow field than is provided by a fine-tuned, simple empirical model. Engineers working continuously with certain kinds of flow fields tend to fine-tune the second-order models as well, without (it is hoped) losing too much of the generality potential within the model.

Perhaps an even more important application of the powerful computation tools available today has been in the rather new field of the numerical simulation of the large eddies of turbulence. In these calculations, the three-dimensional and time-dependent character of the turbulent flow fields is retained. The principal approximations involved in these methods is in the manner of accounting for the scales of turbulence that are too small to be resolved, even in the largest of the computers, for the time-dependent and spatially-dependent boundary conditions, and for the initial field of the turbulence. Because the initial and boundary conditions involve so many degrees of freedom, it cannot be expected that individual computational realizations will be significant or even realistic. What can be expected or at least hoped for is that the results of the computations viewed statistically will accurately reflect the highly nonlinear mechanisms that govern the dynamics of the flows.

The computations, to date, have shown much promise but they need considerable development; moreover, they are much too costly to be considered as engineering tools. They are invaluable, however, as a technique for the study of fluid mechanics in that they yield a mass of information about a flow field that experiments involving discrete numbers of probes cannot possibly provide. The numerical analyst — when faced with making the choices necessary for starting his problem, the ranges of scales he is to examine, and the techniques of accounting for the subgrid scales — is forced to consider the details of turbulence that modelers of statistical turbulence have had to ignore. The apparent turbulence that numerical instabilities or bifurcations can create forces the serious worker in turbulence simulation to continually compare his numerical results with experimental data for similar flow fields. Because of the mass of detail contained within the calculations, where for example any statistical moment can be generated, it is often found that even the classic experiments lack data that unambiguously define the turbulence that was present.

The purpose of this paper is to demonstrate that both methods of turbulence computation have much in common and that they are distinguished primarily by the fraction of the turbulence that is chosen to be modelled. The statistical methods model all of the turbulence, ignoring most of the scale and all of the phase character of the actual turbulence. The large eddy simulations compute the actual physical character of the larger scales of the turbulence and model only those scales of turbulence smaller than the computational mesh dimensions. The fraction of turbulence the subgrid model represents depends largely on the local turbulence Reynolds number and on the number of mesh points that the computer can handle.

In the present discussion, the two methods are interrelated; a review is given of the success or failure of a pair of second-order closure methods to model the statistical properties of a variety of turbulent flow

fields, without adjustment of modelling constants; and some examples of large eddy simulations for simply strained homogeneous turbulent flow fields are presented and compared with data. Examples of statistical model information that can be gained from these computations is shown. Finally, a plea is made for coordinated experiments and large eddy simulations, which together should prove to be most valuable in explaining the physics of turbulence under a variety of flow conditions.

TURBULENT FLOW EQUATIONS

In the analysis of turbulent motions, it is generally believed that the basic physics of the fluid flow is contained within the Navier Stokes equations. Since these same equations apply at a point in space and time for both laminar and turbulent motions, the distinction between these types of flows arises from the initial and boundary conditions the flows experience and from their response to small disturbances that are always present in real flow fields. This response is largely dependent on the Reynolds number of the flow. The properties of turbulence, then, are the consequence of the fluid instabilities that occur at high Reynolds number and the subsequent nonlinear, apparently chaotic, mixing processes that take place. It is these nonlinear processes that produce a broad range of length scales of motion within the turbulent flow and this, in turn, affects finite difference computations greatly.

The length scales range from those comparable to the characteristic dimensions of the apparatus down to those where the turbulent motions have largely been dissipated by viscosity into heat. Even the largest available computers fall far short of being able to resolve such a broad range of scales for flow fields of technological interest. Although the prospects of increasing the resolution of the turbulence scale with future computers is good (Ref. 1), it is not expected that it will be possible to compute the smallest dissipation scales, at Reynolds numbers of interest, in the reasonably near future.

A variety of turbulence models has been developed to account for these small irresolvable subgrid scales. These models have a great deal in common with the models for Reynolds stresses in statistical turbulence theory. This is demonstrated in this section through the equations for an incompressible fluid that describe the small scales of turbulence and their effect on the larger scales and the mean flow.

The instantaneous motion of an incompressible, viscous fluid is described by the continuity and Navier-Stokes equations

$$u_{j,j} = 0 \tag{1}$$

and

$$\dot{u}_i + (u_i u_j + \delta_{ij} p^* - \nu u_{i,j})_{,j} = 0 \tag{2}$$

where

$$p^* = p/\rho \tag{3}$$

The instantaneous, local velocity can be expressed as the sum of three components: the time mean velocity; the sum of the fluctuating turbulence components whose length scales can be resolved by the finite-difference computational scheme; and the sum of those fluctuations too small to be resolved, namely

$$u_i = U_i + \tilde{u}_i + u_i' \tag{4}$$

The other dependent variable, the pressure, can also be resolved in a similar manner

$$p^* = P^* + \tilde{p}^* + p^{*\prime} \tag{5}$$

To convert Eqs. (1) and (2) to contain only resolvable dependent variables, it is necessary to average them or filter them in some manner. For the purposes at hand, it is not necessary to define the filtering process precisely. It can represent a weighted average over a line in space, a surface, a volume, or even a characteristic time comparable to the time scales of the small length scales of turbulence. The filtering process, represented by the symbol $\langle\ \rangle$, will be defined in such a way as to accomplish the following:

$$\left.\begin{aligned} \langle u_i' \rangle &= 0 \\ \langle \tilde{u}_i \rangle &= \tilde{u}_i \\ \langle U_i \rangle &= U_i \\ \langle u_i' U_j \rangle &= 0 \\ \langle u_i' \tilde{u}_j \rangle &= 0 \\ \langle u_{i,j} \rangle &= \langle u_i \rangle_{,j} \end{aligned}\right\} \tag{6}$$

Note that the fourth and fifth definitions in (6) imply that the two scales of turbulence are uncorrelated over the filter domain and that the domain is small compared to the scales of the mean motion. Leonard (Ref. 2) has demonstrated the limitations of these assumptions, but the simplicity resulting from them is attractive for the present development.

With Eq. (4), Eq. (1) becomes

$$U_{j,j} + \tilde{u}_{j,j} + u_{j,j}' = 0 \tag{7}$$

When filtered according to Eq. (6), Eq. (7) reduces to

$$U_{j,j} + \tilde{u}_{j,j} = 0 \tag{8}$$

When Eq. (8) is time-averaged in the Reynolds sense, that is,

$$\bar{f} = \lim_{T\to\infty} \frac{1}{T} \int_0^T f(t)dt \tag{9}$$

there results

$$U_{j,j} = 0 \tag{10}$$

Of course, subtracting Eq. (10) from Eq. (8), and Eq. (8) from Eq. (7) yields

$$\tilde{u}_{j,j} = 0 \tag{11}$$

and

$$u'_{j,j} = 0 \tag{12}$$

Similar operations of filtering and time-averaging on the Navier-Stokes equations (Eq. (2)) yield the following forms of the momentum equation. The mean-momentum equations are

$$U_j U_{i,j} = -\delta_{ij} P^*_{,j} + \nu U_{i,j,j} - (\overline{\tilde{u}_i \tilde{u}_j} + \overline{\langle u'_i u'_j \rangle})_{,j} \tag{13}$$

The momentum equations for the resolvable turbulence scales needed to evaluate the $\tilde{u}_i$ in Eq. (13) are

$$\dot{\tilde{u}}_i + U_j \tilde{u}_{i,j} = -\delta_{ij} \tilde{p}^*_{,j} + \nu \tilde{u}_{i,j,j} - \tilde{u}_j U_{i,j} - (\tilde{u}_i \tilde{u}_j - \overline{\tilde{u}_i \tilde{u}_j})_{,j} - (\langle u'_i u'_j \rangle - \overline{\langle u'_i u'_j \rangle})_{,j} \tag{14}$$

The equations for the instantaneous values of the filtered moments of the subgrid scales, themselves at resolvable scales, can be expressed as

$$\begin{aligned} \langle u'_i \dot{u}'_k \rangle + (U_j + \tilde{u}_j)\langle u'_i u'_k \rangle_{,j} = &-\langle u'_k u'_j \rangle (U_i + \tilde{u}_i)_{,j} - \langle u'_i u'_j \rangle (U_k + \tilde{u}_k)_{,j} \\ &- \langle u'_i u'_k u'_j \rangle_{,j} - \langle u'_k p^{*\prime}_{,i} \rangle - \langle u'_i p^{*\prime}_{,k} \rangle \\ &+ \nu \langle u'_i u'_k \rangle_{,j,j} - 2\nu \langle u'_{k,j} u'_{i,j} \rangle \end{aligned} \tag{15}$$

An equation for the subgrid turbulence kinetic energy, defined as

$$\langle q^2 \rangle = \langle u'_i u'_i \rangle \tag{16}$$

follows from the trace of Eq. (15):

$$\begin{aligned} \langle \dot{q}^2 \rangle + (U_j + \tilde{u}_j)\langle q^2 \rangle_{,j} = &-2\langle u'_i u'_j \rangle (U_i + \tilde{u}_i)_{,j} - \langle u'_j (2p^{*\prime} + q^2) \rangle_{,j} \\ &+ \nu \langle q^2 \rangle_{,j,j} - 2\nu \langle u'_{i,j} u'_{i,j} \rangle \end{aligned} \tag{17}$$

Equation (13) shows that the influence on the mean motion of the two scales of turbulence is through the sum of two Reynolds stresses, each associated with the different scales. In statistical turbulence theory, the different scales of turbulence are ignored by summing these Reynolds stresses into a single stress which is then modelled. Thus, all the effects of the turbulence on the mean motion are modelled. In large eddy simulations, however, the $\tilde{u}_i$ are calculated as functions of time and in three dimensions and the corresponding large eddy Reynolds stresses are then computed through time averaging. (Actually, most large eddy simulations compute the sum of U_i and $\tilde{u}_i$, but in principle the mean flow is affected as stated.) Only the small scales are modelled and their influence is felt on the mean flow through the Reynolds stresses they contribute and in their effect on the larger scales of the turbulence. As the larger fraction of the turbulence spectrum is computed, less reliance has to be placed on contributions of the turbulence model. A mechanism exists, then, for converging on the correct statistical description of turbulence through a systematic increase in the fraction of the resolved turbulence scales. It is not clear, to date, how the quality of the subgrid turbulence model affects this convergence rate and actually how many scales of the large eddies require computation to provide a good description of the turbulence transport mechanism in a variety of flow fields. Another apparent advantage of the method of large eddy simulations is based on the optimism regarding the generation of a universal subgrid model. This optimism reflects the experimental evidence that the small scales of turbulence in a variety of flow fields exhibit similar spectral characteristics when scaled in the Kolmogorov sense.

Equation (14) illustrates the influence of the mean flow and the subgrid turbulence scales on the resolvable scales of the turbulence. It shows that the growth of the resolvable turbulence along a mean streamline is acted on by the turbulence pressure and viscous diffusion in the same manner that the corresponding terms act in the mean flow. The additional last three terms represent the interactions between the resolvable turbulence and the mean flow, the components of the resolvable turbulence, and the subgrid scales of the turbulence. It is the latter terms that must be modelled to close the calculation of the resolvable scales.

Incidentally, these calculations must be performed in three dimensions and in time for each component of the resolvable turbulence; it is a rather costly process on today's computers.

Equations (15) and (17) provide insight into the modelling of the subgrid turbulence scales needed to "close" Eqs. (13) and (14). When either Eq. (15) or Eq. (17) for the subgrid scale moments is compared with the equations representing the Reynolds stresses or kinetic energy in a statistical turbulence formulation, it is noted that they have essentially the same form except that the mean flow in the statistical equations has been replaced by the instantaneous large-scale motions, and the subgrid-scale moments have a time dependence. This strong similarity between the subgrid-moment equations and the Reynolds stress equations suggests that much of the experience gained with statistical modelling procedures eventually will be able to be applied to subgrid modelling. At present, the limitations of computer storage encourage use of the simplest of subgrid models, analogous to the first-order closure methods, such as constant eddy diffusivities or mixing-length models in statistical Reynolds stress methods. Equations (15) and (16), however, suggest that second-order closure methods applied in statistical methods over the past decade will have a role in subgrid closure as well. Computer limitations and costs, also, will restrict large-eddy simulation in the near future to simple flow fields. The results, however, will provide considerable insight into the physics of turbulence and will contribute to modelling of the statistical equations. Some preliminary studies of the latter are given later in this paper.

STATISTICAL TURBULENCE MODELLING

Since the 1968 Stanford conference on the computation of turbulent boundary layers (Ref. 3), statistical turbulence modelling for engineering applications has gone in two directions. The first has been the fine tuning of first-order closure methods, involving algebraic mixing-length models. This was accomplished by fitting the models to well-defined experiments with attached boundary layers experiencing pressure gradients and/or surface mass transfer. References 4 and 5 are examples of this approach. Although these methods yield excellent representations of the data within their range of application, their abilities to extrapolate beyond the ranges of the experiments that form their basis is questionable. Any introduction of additional length scales into the boundary-layer characteristics, such as a transverse radius of curvature comparable to the boundary-layer thickness or an injection slot dimension, requires considerable remodelling of the length scales. In the absence of experimental guidance, this remodelling has to be based on ad hoc assumptions. Further, in flow fields where changes in the mean flow are rapid, the assumption inherent in most first-order closure methods, that the turbulence remains in equilibrium with the mean flow, may not be true. The recognition of these limitations of first-order closure methods has led to considerable work in the second direction, namely second-order closure methods, where one or more of the characteristics of turbulence is represented by a partial differential transport equation. These methods are based largely on the concepts presented in the pioneering papers by Kolmogorov (Ref. 6), Chou (Ref. 7), and Rotta (Refs. 8,9). As explained in the Introduction, the impetus behind the development of second-order closure methods was the belief that they have the potential of a broad range of applicability and may, with further development, become predictive tools in engineering computations.

An ideal predictive turbulence model would be one that could remain unaltered in form and in its empirical coefficients for all flow fields. It is questionable, however, that such an ideal universal model can be achieved within the framework of statistical models, even when allowance is made for acceptable engineering error. Such models inherently ignore spectral and phase relationships between eddies of different sizes. The larger eddies in a turbulent flow are known to reflect the particular nature of the flow and this alone is sufficient to raise doubts regarding the potential universality of statistical models. Of course, zonal turbulence models that differ from flow to flow but can be related to some particular mean flow feature are also of value to the design engineer; they may be the best that can be expected of statistical models. Such zonal models, however, introduce mathematical difficulties in the identification of the bounds of different zones of applicability of the individual models, and the means of coupling the interaction between these zones. It is much easier to deal with the same model throughout the flow. In view of this, it would be illuminating to learn how well or how poorly a fixed model could work on a variety of boundary-layer flows. To demonstrate this, calculations based on a pair of fixed second-order closure models will be compared here with data from a variety of experiments.

The particular models chosen for this comparison have been developed for the most part by Wilcox and Traci (Ref. 10) with some collaboration by the present author (Ref. 11), and were an outgrowth of the early work of Saffman (Ref. 12). One model uses an eddy viscosity, which is dependent on the kinetic energy of turbulence and the dissipation rate per unit of kinetic energy (a specific dissipation rate or Saffman's "pseudovorticity"). The other model closes the Reynolds stress equations directly, with the scale of turbulence again being defined with the specific dissipation rate. In choosing these models for comparison here, the author does not wish to imply that he believes them to be the best of the second-order closure methods available today to represent boundary-layer flows. In some respects, the models developed by Launder and his colleagues (Refs. 13,14) are more general and represent the mean flow very close to a surface in a more realistic manner (Refs. 14,15). On the other hand, computations of some compressible flow fields with two-equation models favor the Wilcox-Rubesin model (Ref. 11). It is not clear at present which, if any, existing model will be most uniformly valid for all applications. The primary reason for presenting models in which the author was involved was his access to computer codes containing them; as a result, the codes could be used to generate the examples that follow. Also, since both of these models and those identified with Launder utilize essentially the same data to establish their modelling coefficients, it should not make much difference in the examination of the universality of second-order closure modelling of boundary-layer flows which family of models is employed.

Mean Flow Equations and Boundary Conditions

The mean flow equations used in computing the examples that will be treated later are written for a compressible fluid in mass-weighted-average dependent variables (Ref. 16). The conservation equations for mass, momentum, and energy are as follows:

$$\dot{\rho} + (\rho u_j)_{,j} = 0 \tag{18}$$

$$(\dot{\rho u_i}) + (\rho u_j u_i)_{,j} = -p_{,i} + (\rho \tau_{ij}^T)_{,j} \tag{19}$$

$$(\dot{\rho h}) + (\rho u_j h)_{,j} = \dot{p} + u_j p_{,j} + \rho \tau_{ij}^T u_{i,j} - (\rho Q_j^T)_{,j} \tag{20}$$

Here, the symbols τ_{ij}^T and Q_j^T denote the specific mass-weighted-average total shear stress and heat flux that include the contributions of both the molecular and turbulent transport. These quantities are defined as

$$\tau_{ij}^T = 2\nu S_{ij} - \frac{1}{3} u_{k,k} \delta_{ij} + \tau_{ij} \tag{21}$$

and

$$Q_j^T = -\frac{\nu}{Pr_L} h_{,j} + Q_j \tag{22}$$

the mean rate of strain tensor in Eq. (21) is

$$S_{ij} = \frac{1}{2} (u_{i,j} + u_{j,i}) \tag{23}$$

Finally, τ_{ij} and Q_j are the mass-weighted-averaged Reynolds stress tensor and heat flux vector defined by

$$\left.\begin{aligned} \tau_{ij} &= -\frac{\langle \tilde{\rho} u_i'' u_j'' \rangle}{\rho} \\ Q_j &= \frac{\langle \tilde{\rho} u_j'' h'' \rangle}{\rho} \end{aligned}\right\} \tag{24}$$

where $\tilde{\rho}$ is the instantaneous density, $\langle \theta \rangle$ denotes the time average of θ, and θ'' is the fluctuating part of θ in mass-weighted-average formulation. The surface boundary conditions for Eqs. (18) to (20) are:

at $x_2 = 0$

$$\left.\begin{aligned} u_1 &= 0 \\ u_2 &= 0 \quad \text{or} \quad v_w(x_1) \\ h &= h_w(x_1) \quad \text{or} \quad (\partial h/\partial x_2) = (\partial h/\partial x_2)_w \end{aligned}\right\} \tag{25}$$

All flow variables approach free-stream flow conditions in general flow-field computations. For the special case of two-dimensional boundary layers, boundary conditions at the boundary-layer edge are

at $x_2 = \delta(x_1)$

$$\left.\begin{aligned} u_1 &= U_e(x_1) \\ h &= h_e(x_1) \end{aligned}\right\} \tag{26}$$

The two models used to close these equations are given in the following sections.

Two-Equation Eddy-Diffusivity Model

The two-equation model considered here utilizes an eddy diffusivity defined as

$$\varepsilon = \gamma^* e/\omega \tag{27}$$

where the turbulence kinetic energy e and specific dissipation rate ω are given by the turbulence modelling equations:

$$(\dot{\rho e}) + (\rho u_j e)_{,j} = \rho \tau_{ij} u_{i,j} - \beta^* \rho \omega e + [(\mu + \sigma^* \rho \varepsilon) e k_j]_{,j} \tag{28}$$

and

$$(\dot{\rho \omega^2}) + (\rho u_j \omega^2)_{,j} = \gamma \frac{\omega^2}{e} \rho \tau_{ij} u_{i,j} - [\beta + 2\sigma(\ell_{,k} \ell_{,k})] \rho \omega^3 + [(\mu + \sigma \rho \varepsilon)(\omega^2)_{,j}]_{,j} \tag{29}$$

To account for compressibility, all the dependent variables are expressed as mass-weighted averages (Ref. 16). The length scale is represented by

$$\ell = \frac{e^{1/2}}{\omega} \tag{30}$$

The modelling closure coefficients employed are as follows

$$\left.\begin{aligned} &\beta = 3/20,\ \beta^* = 9/100,\ \sigma = \sigma^* = 1/2 \\ &\gamma^* = [1 - (1 - \lambda^2)\exp(-Re_T/R_e)] \\ &\gamma\gamma^* = \gamma_\infty[1 - (1 - \lambda^2)\exp(-Re_T/R_\omega)] \\ &\gamma_\infty = 10/9,\ \lambda = 1/11,\ R_e = 1,\ R_\omega = 2 \end{aligned}\right\} \tag{31}$$

The Reynolds number of turbulence is given by

$$Re_T = \frac{e^{1/2}\ell}{\nu} \tag{32}$$

The boundary conditions appropriate to these modelling equations, when they are applied to boundary layers, have been guided by asymptotic analysis and reference to other models. The surface boundary conditions for Eqs. (19) and (20) are as follows:

at $x_2 = 0$

$$\left.\begin{aligned} e &= 0 \\ \omega &\to \frac{20\ \nu_w}{\beta x_2{}^2} \end{aligned}\right\} \tag{33a}$$

at $x_2 = \delta(x_1)$

$$\left.\begin{aligned} e &= \imath U_e{}^2(x_1) \\ \ell &= 0.09\ \beta^{*1/4}\delta(x_1) \end{aligned}\right\} \tag{33b}$$

As the quantity $\ell/\beta^{*1/4}$ behaves much like the classical mixing length, the proportionality coefficient of 0.09 in Eq. (19) is readily seen to be consistent with the Escudier eddy-viscosity model (Ref. 17).

Since it was desired to model Reynolds stresses that do not necessarily align with the mean rates of strain, the constitutive relationship relating these quantities was written as

$$\tau_{ij} = \frac{2}{3}\,e\delta_{ij} + 2\varepsilon\left(S_{ij} - \frac{1}{3}\,u_{k,k}\delta_{ij}\right) + \frac{8}{9}\,\frac{e}{(\beta^*\omega^2 + 2S_{mn}S_{nm})}\,(S_{im}\Omega_{mj} + S_{jm}\Omega_{mi}) \tag{34}$$

where the third term on the right was guided by the work of Saffman (Ref. 18). The vorticity tensor used here is defined as

$$\Omega_{ij} = \frac{1}{2}\,(u_{i,j} - u_{j,i}) \tag{35}$$

and the mean rate of strain is given by Eq. (23).

Reynolds Stress Equation Model

The modelling in the Reynolds stress equations (RSE) presented here utilizes (1) a particular version of the pressure rate-of-strain correlation presented by Launder et al. in Ref. 14, (2) gradient diffusion for third-order correlations involving velocity and pressure, and (3) isotropic dissipation. Following Launder et al., the pressure rate-of-strain correlation is represented as

$$\overline{p(u_{i,j} + u_{j,i})} = C_1\beta^*\omega\left(\tau_{ij} + \frac{2}{3}\,\delta_{ij}e\right) - \hat{\alpha}\left(P_{ij} - \frac{2}{3}\,P\delta_{ij}\right) - \hat{\beta}\left(D_{ij} - \frac{2}{3}\,P\delta_{ij}\right) - \hat{\gamma}eS_{ij} \tag{36}$$

where the first term on the right, called the Rotta term, is proportional to the anisotropy of the turbulence. The terms preceded by the modelling coefficients $\hat{\alpha}$, $\hat{\beta}$, and $\hat{\gamma}$ are contributed by the interaction of turbulence and mean flow expressed in terms of

$$\left.\begin{aligned} P_{ij} &= \tau_{ik}u_{j,k} + \tau_{jk}u_{i,k} \\ D_{ij} &= \tau_{ik}u_{k,j} + \tau_{jk}u_{k,i} \\ P &= \frac{1}{2}\,P_{ij} = \frac{1}{2}\,D_{ii} = \tau_{mn}S_{nm} \end{aligned}\right\} \tag{37}$$

In choosing the values of $\hat{\alpha}$, $\hat{\beta}$, $\hat{\gamma}$, Wilcox and the author opted to rely on experimental data rather than the symmetry arguments recommended by Rotta (Ref. 8) and carried out by Launder et al. (Ref. 14). The first experimental observation employed was that

$$\tau_{33} \cong \frac{1}{2}\,(\tau_{11} + \tau_{zz}) \tag{38}$$

when a homogeneous turbulent flow is equally stretched in the x_1 direction and compressed in the x_2 direction, which by continuity in an incompressible fluid leaves the x_3 direction unstrained (Ref. 19). The second observation was that a field of homogeneous turbulence in rigid body rotation decays without developing anisotropy (Ref. 20). The latter data forces $\hat{\alpha} = \hat{\beta}$. The remaining constants are evaluated, after representative values of τ_{22}/τ_{11} and τ_{12}/e are established from data in a homogeneous shear flow or in the law-of-the-wall region of a flat-plate boundary layer. The model used here was based on the approximate relationships $\tau_{22}/\tau_{11} \cong 1/2$ and $\tau_{12}/e = 0.3$, both of which are consistent with the form of the two-equation model in shear flow. Further remarks regarding the modelling constants found in this way will be made in the section on large eddy simulations.

With the modelling described, the Reynolds stress equations expressed in terms of the components of Reynolds stress are

$$(\rho\dot{\tau}_{ij}) + (\rho u_k \tau_{ij})_{,k} = -\rho\tau_{im}u_{j,m} - \rho\tau_{jm}u_{i,m} + \frac{2}{3}\beta^*\rho\omega e\delta_{ij} - C_1\beta^*\rho\omega\left(\tau_{ij} + \frac{2}{3}e\delta_{ij}\right)$$
$$+ \rho\left(\tau_{jm}S_{mi} + \tau_{im}S_{mj} - \frac{2}{3}\tau_{mn}S_{nm}\delta_{ij}\right) + \frac{4}{3}\rho e\left(S_{ij} - \frac{1}{3}u_{k,k}\delta_{ij}\right) + [(\mu + \sigma^*\rho e)\tau_{ij,k}]_{,k} \tag{39}$$

The components of the Reynolds heat flux are modelled with

$$(\rho\dot{Q}_i) + (\rho u_j Q_i)_{,j} = \rho\tau_{ij}h_{,j} - \rho Q_j u_{i,j} - \beta^{**}\rho\omega Q_i + \left[\left(\frac{\mu}{Pr_L} + \sigma^{**}\rho\varepsilon\right)Q_{i,j}\right]_{,j} \tag{40}$$

The specific dissipation rate used to provide the scale of the turbulence is again given by Eq. (20). In these equations

$$\varepsilon = e/\omega$$
$$e = -\frac{1}{2}\tau_{ii} \tag{41}$$

and the modelling coefficients are

$$\left.\begin{aligned}
&\beta = \frac{3}{20}\,,\quad \beta^* = \frac{9}{100}\,,\quad \beta^{**} = \frac{9}{25}\,,\quad \sigma = \sigma^* = \frac{1}{2}\,,\quad \sigma^{**} = 2\\
&C_1 = C_{1_\infty}\left[1 - (1 - \lambda^2)\exp\left(\frac{-Re_T}{R_e}\right)\right]^{-1}\\
&\frac{\gamma}{C_1} = \frac{\gamma_\infty}{C_{1_\infty}}\left[1 - (1 - \lambda^2)\exp\left(\frac{-Re_T}{R_\omega}\right)\right]\\
&C_{1_\infty} = \left[\frac{9}{2} - \frac{5}{2}\exp(-5\chi)\right]\\
&\gamma_\infty = \frac{13}{11}\,,\quad \lambda = \frac{1}{14}\,,\quad R_e = 1\,,\quad R_\omega = 3
\end{aligned}\right\} \tag{42}$$

where

$$\chi = \sqrt{\frac{2S_{mn}S_{nm}}{\beta^*\omega^2}}$$

Again, the Reynolds number of turbulence Re_T is given by Eqs. (30) and (32). At the solid surface, Eqs. (24) again apply and, in addition

at $x_2 = 0$

$$\left.\begin{aligned}
Q_j &= 0\\
\tau_{ij} &= 0
\end{aligned}\right\} \tag{43}$$

At the boundary-layer edge, in addition to Eqs. (24), it is required that

at $x_2 = \delta$

$$\left.\begin{aligned}
Q_j &= 0\\
\tau_{ij} &= \frac{2}{3}\iota U_e^2(x_1)\delta_{ij}
\end{aligned}\right\} \tag{44}$$

Examples of Turbulence Model Application

As an initial example of the use of the turbulence models presented here, consideration is given to the distortion of a field of fully developed, homogeneous turbulence by application of plane or normal strains. This case acts as a test of the models when near-surface effects are absent. The particular case treated

corresponds to the flow in the experiment by Tucker and Reynolds (Ref. 19). Figure 1 shows a schematic diagram of the test channel. The fluid enters at the left, is conditioned through screens, and passes toward the right in parallel flow until it reaches the station where the constant rate of strain is applied. The constant strain is achieved by exponentially expanding the channel in the x direction and contracting it in the y direction so as to maintain a constant cross-sectional area. The straining causes the initially nearly isotropic turbulence to become anisotropic, a measure of which is the straining parameter plotted as the ordinate in the lower portion of the figure. After the fluid is strained, it is returned to a parallel flow. Here the fluid tends to return to isotropy.

Use of the RSE model in computing this flow is noted to yield reasonably good agreement with the data. At the initiation of straining, the computed growth of anisotropy is somewhat faster than the data, but this trend reverses toward the end of the straining region and downstream. These trends were influenced by the assumed form of $C_{1\infty}$ in Eq. (42) which was adjusted to fit an aggregate of homogeneous flow experiments, not just that of Tucker and Reynolds. Use of the two-equation model in the computations suffers in two respects. First, the model shows the difficulties of all eddy viscosity models when a sudden application or removal of mean strain occurs. Although the elements making up the eddy viscosity (ℓ and ω) vary continuously where the discontinuities in strain occur, the corresponding Reynolds stresses are still discontinuous. Second, the rate of generation of anisotropy, by the two-equation model away from the stations where the discontinuities occurred, was too slow. Thus, although the RSE model has been shown to yield rather good agreement with the data, this example illustrates that two-equation models are limited to flow conditions with more gradual application of mean strain.

An example of the application of the turbulence models to a boundary-layer flow of an incompressible fluid is demonstrated in Figs. 2 through 4. The data are from the experiment conducted by Bradshaw in which a turbulent boundary layer was exposed to a sudden application of an adverse pressure gradient (Ref. 21). The data points designated with open symbols result from a reinterpretation of the basic data by an independent analysis (Ref. 22) and provide an indication of the uncertainty inherent in the data. Figure 2 shows the distribution of skin friction and boundary-layer shape factor along the test zone. The computations were started by matching the momentum-thickness Reynolds number from a flat-plate calculation to the Reynolds number measured at the upstream station. Beyond this station, the experimental pressure distributions were imposed on the boundary-layer calculations. It is observed that the two-equation model and the Reynolds-stress model both yield skin friction and shape factor results that are nearly the same, and that both agree well with the data. It should be noted that no adjustments were made to the modelling to account for the pressure gradient.

The measured and computed mean-velocity profiles at the farthest downstream station are shown in Fig. 3, which is expressed in wall-law coordinates. The computations based on both models yield results in good agreement with the data. In the "law-of-the-wall" region, the computed results agree with the standard logarithmic formula. In that region, also, there is a little better agreement with Coles' reinterpretation of the data (Ref. 22). Neither of these observations is surprising, as the use of the logarithmic law with the constants shown played a major role in the data reinterpretation and in establishing some of the modelling coefficients used in both models. Perhaps more significant is that the computed results based on both models show the enhanced contribution of the "wake" region that is characteristic of boundary-layer flows in adverse pressure gradients.

Figure 4 compares the Reynolds stress, turbulence energy, and mean-velocity profiles, computed from the two models, with Bradshaw's data. In these figures, the distance normal to the surface has been normalized by the boundary-layer thickness. Generally, the Reynolds stress components and the turbulent kinetic energy given by the two models differ less from each other than from the data. The normal components of Reynolds stress — $\langle u'^2 \rangle$, $\langle w'^2 \rangle$ and, to a lesser degree, the kinetic energy — are evaluated rather poorly in the inner half of the boundary layer. On the other hand, the normal Reynolds stress $\langle v'^2 \rangle$ and the shear stress $\langle -u'v' \rangle$ fit the data much better. This reflects the adjustment of some of the modelling coefficients to provide good mean-velocity profiles in a flat-plate boundary layer, where a good evaluation of the Reynolds shear stress is paramount. In the coordinates of this figure, the two-equation model shows a little advantage over the RSE model; however, both models yield results that reflect the "flattening" of the velocity profile introduced by the adverse pressure gradient.

The results that have been shown here are representative of comparisons of many other sets of data with computed results based on the two models. For attached, subsonic boundary layers on flat plates, with or without pressure gradients, there seems to be no advantage to the Reynolds stress model. Under these flow conditions, the departure of the turbulence from being in equilibrium with the mean flow is apparently too small to cause the two-equation model difficulties that were indicated earlier with suddenly distorted homogeneous flows.

The growth of a turbulent boundary layer on a small-radius circular cylinder with its axis parallel to the free stream is an example of a flow where the mixing-length formulation required considerable change, from that on a flat plate, to make computations conform with the experimental results. Generally, the data showed that as the ratio of the boundary-layer thickness to the transverse radius increased, the "wake" region of the boundary layer diminished (as occurs on a flat plate in a favorable pressure gradient). Also the skin-friction coefficient at a given Reynolds number based on boundary-layer thickness increased with diminishing body radius. When Rao (Ref. 23) examined this flow field, he concluded that conformance with his data could be achieved if he employed a wall-region law equivalent to setting the mixing length in the inner region of the boundary layer to

$$\ell_m = ky \left[\frac{\ell n(1 + y/a)\sqrt{1 + y/a}}{(y/a)} \right] \tag{45}$$

In studying the same problem, Richmond (Ref. 24) deduced a formulation equivalent to

$$\ell_m = ky \left[\frac{(1 + y/2a)}{(1 + y/a)^{3/2}} \right] \tag{46}$$

For values of $y \approx a$, Eq. (45) remains within a few percent of $\ell_m = ky$, whereas Eq. (46) shows a reduction of about 50%. These differences result in adjusting the position of data in opposite directions, in terms of y^+, relative to the universal "law of the wall" and demonstrates vividly how arbitrary the extensions of mixing-length closure can be.

The RSE second-order closure model given here was applied without change to this type of flow to see if the experimental data could be represented. Figure 5 compares the computed results and measured data in terms of the effect on skin friction of the ratio of δ/a. Four sets of data are utilized (Refs. 24-27) to cover a sizable δ/a range. The computational results are shown as a band because the ordinate employed does not collapse all of the Reynolds number dependence. The computations with the unchanged RSE model represent the trends of the data well up to a value of $\delta/a = 10$, where the C_f is 30% higher than that on a flat plate. Beyond this, a significant departure occurs from the data of Willmarth et al. (Ref. 27) where the measured C_f is increased to more than twice that of a flat plate. Apparently, the RSE model in its present form fails to fully account for changes in the wake character of the boundary layer over a body with an extremely small transverse radius.

The next example to be treated deals with the topic of streamwise curvature, the importance of which was first recognized by Bradshaw (Ref. 28). The Reynolds-stress equations were applied to this problem directly through the conversion of the coordinates from Cartesian to curvalinear, with one axis tangent to the surface, s, and the other normal to the surface, n. The two-equation model, however, required reinterpretation of the meaning of the symbol e, treated as the kinetic energy earlier. Details of these transformations are given in Ref. 11.

For flow over a streamwise curved surface, the s, or curvilinear coordinate system, introduces terms in the Reynolds stress equations analogous to centrifugal and Coriolis forces in the momentum equations. When the normal stresses are added together, however, most of these additional terms cancel, resulting in an energy equation that is essentially the same as on a flat surface; the only change is in the production term where the mean-velocity gradient $\partial u/\partial y$ is replaced by $(\partial u/\partial r) - (u/R)$. The specific energy-dissipation-rate equation is also changed in the same way. Thus, a direct application of the two-equation model as given earlier would not show streamline curvature effects of the magnitude indicated by a Reynolds stress model or by the experimental data (e.g., Ref. 29). This deficiency was corrected by (1) observing that the Reynolds shear stress and $\overline{v'^2}$ equations in the RSE model in s, n coordinates added similar terms because of the streamwise curvature and (2) identifying e with a "mixing energy" rather than a "kinetic energy." The symbol e then is redefined as

$$e = + \frac{9}{4}\overline{v'^2} = - \frac{9}{4}\tau_{nn} \tag{47}$$

which follows from the basic model in a homogeneous shear flow where the turbulence production and dissipation are in balance. With Eq. (47) and the Reynolds stress equation for $\overline{v'^2}$ and $\overline{u'v'}$ as guides, the e equation for use with the two-equation model only is written in an ad hoc manner as

$$ue_{,s} + ve_{,n} + \frac{9}{2}\frac{u}{R}\tau = \tau\left(u_{,n} - \frac{u}{R}\right) - \beta^* e\omega + [\nu + \sigma^*\varepsilon)e_{,n}]_{,n} \tag{48}$$

with

$$\tau = \varepsilon\left(u_{,n} - \frac{u}{R}\right) \tag{49}$$

and, where ε follows from Eq. (27); all the modelling coefficients and relationships employed in the two-equation model introduced earlier are retained. The third term on the left side of Eq. (48) represents the principal extra rate of turbulence production introduced by the longitudinal surface curvature.

Calculations based on these model modifications for streamline surface curvature are compared in Fig. 6 with data obtained by So and Mellor (Ref. 29) for a boundary layer on a convex wall with an adverse pressure gradient. The data represent the surface skin-friction coefficient and shape factor along the surface. The computations include the RSE and two-equation models, both with and without the corrections for longitudinal surface curvature. The computed results were matched to the first station by assuming the flow upstream of the station to be on a flat plate of a length to yield the correct skin friction there. The calculations with the RSE or two-equation model unmodified for streamwise curvature show little of the drop in skin-friction coefficient experienced in the experiment. The modified models, on the other hand, give an excellent representation of the skin-friction behavior. This is rather remarkable for the two-equation model, when its ad hoc formulation is considered. Finally, both modified models represent the form factor data also quite well.

It may seem to be illogical in the test of the universality of a turbulence model to make the modifications indicated for introducing the effects of streamwise curvature. For the RSE model, the modifications were purely geometric and were introduced by selecting the appropriate coordinates for the problem considered. No physical modelling changes were made. The original two-equation model, on the other hand, was insensitive to changes in the coordinate system and an extra production term had to be added to the e equation. One can view the need for the change as an indication of the inherent weakness of the original two-equation model, or the view of the final e equation as the basic boundary-layer model that then is simplified geometrically for planar surfaces.

The remainder of the two-dimensional boundary layers considered here involve compressible flows. As noted earlier, the extension to compressible flows is achieved by adopting dependent variables that are Favre mass-weighted averages. In these variables, the conservation equations take forms that avoid terms that are explicitly dependent on the turbulent density fluctuations. Term-by-term, the equations are comparable to their incompressible counterparts, with the compressibility entering only through the mean density variations. Although Favre averaged-model equations are, in the main, parallel term-by-term to their incompressible counterparts, they have additional terms explicitly dependent on density fluctuations that require additional

modelling (Refs. 30,31). In practice, however, it was found that these additional terms could be ignored, even under conditions involving large pressure gradients where the terms are their largest (Ref. 32). Reflecting this, the models presented here neglect these additional terms.

These models were applied to the calculation of skin friction on a cooled flat plate in airflow at a Mach number of 5. The results of these calculations based on the two models are compared with values given by the van Driest II formulas in Fig. 7. These formulas have been shown (Ref. 33) to represent the bulk of existing data under these conditions to about ±10%. The agreement between all the methods is excellent, but this is not surprising in view of the similarity of the density scaling in Favre averaging (Ref. 11) and that which is inherent in the van Driest formulation.

Compressible turbulent boundary layers experiencing severe pressure gradients are cases where the models are tested more severely. The first example of such a flow is the experiment conducted by Lewis et al. (Ref. 34) at a Mach number of four. In that experiment, an axisymmetric turbulent boundary layer on the adiabatic interior wall of a circular cylinder was subjected to an adverse pressure gradient followed by a favorable pressure gradient. The pressure gradients were achieved by means of a shaped center-body; a pressure rise of 9 times the upstream pressure was attained before pressure relaxation occurred. Figure 8 shows the distribution of the surface skin-friction coefficient within the test zone. The coefficient shown is defined in terms of the upstream boundary-layer edge conditions, not the local, and is therefore proportional to the surface shear. The Reynolds number at the initial station was about 7×10^6. Along with the computed results based on the models presented here, computations based on the Marvin Shaeffer code (Ref. 35), which has been extended to contain a classic mixing-length model essentially identical to that of Cebeci (Ref. 4), are given for comparison. The mixing-length model fails to capture the full rise of the skin friction caused by the adverse pressure gradient. On the other hand, it follows the data in the region of favorable pressure gradient quite well. The second-order closure models demonstrate a much better prediction of the rise in skin friction in the adverse pressure gradient region; however, in the following favorable pressure gradient region they show somewhat too large a drop in the skin friction. The two second-order models yield essentially equivalent results.

Figure 9 shows data from a similar experiment conducted by Horstman et al. (Ref. 36) at an initial Mach number of 2.3 and over a large range of Reynolds numbers. In addition to computations based on the two models considered here, computed results from two versions of a mixing-length model and another two-equation model are also shown here. At this Mach number, $M_\infty = 2.3$, the onset of an adverse pressure gradient first reduces the skin friction before a rise similar to that which occurred in Fig. 8 also occurs. Generally, the computed values of skin friction from all the models conform to the trends in the data caused by the change in Reynolds number and the effective pressure gradient. One exception is the behavior of the mixing-length model unmodified for pressure gradient which indicates separation at the lowest Reynolds number. At the higher Reynolds numbers, the difference between the modified and unmodified mixing-length model become very small. From this figure, conclusions regarding the relative merits of the different models would be indecisive. In Fig. 10, when the adverse pressure gradient is applied over a greater distance, the models behave in a somewhat different manner. At the lowest Reynolds number, the unmodified mixing-length model no longer indicates separation. Also, at the lower Reynolds numbers, the second-order closure models are in much better agreement with the data. Omission of the explicit density fluctuation terms resulting in the model equations after Favre averaging is justified by these examples. Incidentally, the computed results labeled Aeronautical Research Associates of Princeton (ARAP) are based on a Reynolds stress model utilizing primitive dependent variables including the whole gamut of fluctuating density terms (Ref. 37).

The remaining examples of two-dimensional boundary layer and near-wake flows were computed with the compressible Navier-Stokes equations to account for strong interactions between the shear layers and the inviscid flow. Because these codes are costly to operate they have been limited, at least to date, to contain models of turbulence of the two-equation kind or simpler. Therefore, the RSE model will not appear in these examples.

Figure 11 shows calculations of the surface pressure and skin-friction distributions compared with data in the region of the interaction of a normal shock wave with a fully established turbulent boundary layer (Ref. 38). The schematic diagram shows that the flow field was developed on the surface of a tube within a slightly supersonic main flow. A normal shock wave was generated and positioned along the test section with a variable blockage device at the downstream end of the test section. The figure at the left shows that the computational results based on the two-equation model generally agree well with the measured surface pressure distributions at the five Mach numbers tested. The departures that exist from the data are small and inconsistent enough to hide any systematic deficiencies in the computational model. The computed skin-friction coefficients again conform to the main features of the data. The calculations show a downstream movement of the minimum in skin-friction coefficient with increasing Mach number. If the extreme Mach number cases are emphasized, a similar movement is seen in the data, although of larger extent. The inaccuracies inherent in skin-friction measurements can possibly exaggerate the movement of the minimum skin-friction coefficient and could be the source of these differences.

An example of a strong interaction between a boundary layer and a shock wave at higher Mach number is the experiment of Settles et al. (Ref. 39) with a turbulent boundary layer traversing a compression corner. The computations used for comparison with the data are from Ref. 40. Figure 12 shows computations and measurements of surface pressure and surface skin friction for two deflection angles of the compression corner, $\alpha = 20°$ and $24°$. Besides the two-equation model under consideration, three other models have been used in these computations. Models not shown in any of the earlier examples are a kinetic energy model with an algebraic length scale (Ref. 31) and the Jones-Launder two-equation model (Ref. 13). A general observation is that both two-equation models yield essentially the same results, except for the level of skin friction in the reversed region. This suggests the kinds of measurement needed to distinguish between models. Comparison of the experimental data with the computations reveals that the two-equation models permitted the location of the onset of the increased surface pressure ahead of the compression corner to be computed quite well. For $\alpha = 20°$, these models yield excellent pressure distributions over the separated zone and on the deflected surface beyond reattachment. For $\alpha = 24°$, the calculated pressure in the separated zone is somewhat high, although ahead of separation and after reattachment the pressure is again evaluated quite well.

The zero-equation and one-equation models show late onsets of pressure rise, then overshoot the data, and then blend with the data far downstream. The comparison with the skin-friction data do not show all the same trends in the computations with the different models. The two-equation models define the position of the onset of the fall-off of skin friction, and the other models again lag this. The fall-off of the skin friction given by the two-equation models is faster than the data show, so that the points of separation are predicted upstream of where they actually are. The two-equation models also yield too long a separated region so that reattachment is calculated to be downstream of the experimental results. The comparison is inconclusive, regarding which of the models best fits the downstream data, except that the algebraic model yields results that consistently fall lower than the data.

Figure 13 compares the computations and measurements of the effect of Reynolds number on the extent of the upstream pressure influence ahead of the compression corner. The distances considered are shown schematically in the left-hand sketch in Fig. 13. Two deflection angles are considered: $\alpha = 16°$ and $\alpha = 20°$. It is seen that the observation made earlier that the two-equation models evaluate the position of the onset of the pressure rise best is borne out in the figure over the entire range of Reynolds number covered in the experiment.

Another example in which computations with the two-equation model have been compared with experimental data is the work by Viswanath et al. (Ref. 40). The experiment was conducted at the trailing edge of a flat-plate test model that terminated with a 12.5° total included angle wedge. In the example cited here, the model and wedge trailing edge were both kept at zero angle of attack to an airstream at $M = 0.7$. Figure 14 compares measurements of the mean-velocity profiles just upstream and downstream of the trailing edge with computations employing the two-equation model and an algebraic model (Ref. 4) in both Navier-Stokes and boundary-layer equation. The high chord Reynolds number of 40×10^6 ensured a fully turbulent boundary layer well ahead of the trailing edge. In this figure, θ_0 represents the momentum thickness of the boundary layer 0.4 cm upstream of the trailing edge; it is equal to 0.2 cm. The computations employing either model in the Navier-Stokes equations agree better with the data than the same models in the boundary-layer computations. Under these conditions, either on the wedge or just beyond the trailing edge, the flow is more sensitive to the interaction between the shear flow and the inviscid flow regions than to the particular turbulence model. Apparently the rate of change of the mean motion, even this close to the trailing edge, is sufficiently slow for either an equilibrium-model or a two-equation model to still apply. Farther downstream in the wake, both models and both computation techniques yield essentially the same results. It is important to note that the sudden removal of a surface downstream of the trailing edge did not cause any difficulties with the near-wall modifications represented by Eqs. (31), as they blended smoothly toward their asymptotic values farther in the wake.

The final example cited here is the response of a turbulent boundary layer to a sudden application of transverse shear, as studied experimentally on an axisymmetric rotating body in Refs. 25 and 26. A sketch of the model configuration is given in Fig. 15. The free-stream velocities in these experiments ranged from 10 to 19 m/sec. A comparison of the data from the two experiments with a mixing-length model (Ref. 42) modified with Eq. (45), the two-equation and RSE models, and the ARAP model (Ref. 37) has been represented in Ref. 43. In the computations with either of the eddy-viscosity models, it was necessary to introduce an additional assumption regarding the ratio of the eddy diffusivity corresponding to the transverse flow to that of the longitudinal flow. The need for assuming some value for the ratio is an inherent problem in the application of any scalar eddy-viscosity model to a three-dimensional boundary layer. In the computations with the two-equation model, this ratio was set equal to unity, as it was for the mixing-length model in Ref. 42. It was found in Ref. 43 that computations based on the simple mixing-length model yielded results in general agreement with the measurements of the mean flow. The two-equation and RSE models showed comparisons that were only somewhat better than the simpler model. The improvement achieved by the second-order closure models seemed to be limited by too rapid a response to the transverse shear. The relative agreement between the RSE model and the scalar eddy-viscosity models can be explained by reference to Fig. 15 where the ratio of the eddy viscosities calculated from the RSE model are compared to the data from the two experiments. First, it is observed that the two similar experiments result in data in serious disagreement. The appropriate ratio cannot be established experimentally. The RSE model, with or without the effects introduced by transverse curvature, shows that the ratio of eddy viscosities remains within ±10% of unity over most of the transverse boundary layer, as assumed in the eddy-viscosity models. Near the outermost edge of the transverse boundary layer, in the vicinity of the onset of the transverse shear, the ratio drops to a smaller number. As there is little momentum change near the boundary-layer edge, differences in eddy viscosity such as these have negligible effect on the transverse-velocity profiles. Thus, the choice of the eddy viscosity ratio of unity in the simpler models is not inconsistent with the evaluation of the RSE model.

Concluding Remarks Regarding Statistical Modelling

From the foregoing set of comparisons of experimental data and computations employing a pair of fixed second-order closure models, and with other models as well, it is observed that the second-order closure models generally have a broader range of application than do the algebraic closure models. The two-equation eddy-viscosity model is accurate over a large range of Reynolds numbers for attached two-dimensional incompressible or compressible boundary layers on impervious surfaces, even those with small zones of separation. The Reynolds stress model, in addition, has advantages when sudden changes in the mean flow occur, for surfaces with streamwise curvature, and in three-dimensional boundary layers. Both models show the Favre mass-weighted dependent variables account well for compressibility, even with rather large $\partial p/\partial x$, and also can account for modest effects of transverse curvature.

These models still require adjustments to increase their breadth of application. For example, the two-equation model needs an extra rate of strain added to the mixing-energy equation to account for the effect of streamwise curvature on a boundary layer. This ad hoc correction is very successful, practically, for boundary-layer calculations. In the Navier-Stokes form of the model, however, it has not yet been made to account for rapid turning within a flow. Nevertheless, the trailing-edge example cited did not seem to need this correction. Both models are unable to completely relaminarize an incompressible boundary layer in strong favorable pressure gradient. This is not a general failure of second-order models; another second-order closure model (Ref. 13) has been somewhat more successful in accounting for relaminarization than the models given here. Both models also require major changes in their surface boundary conditions to account for surface mass transfer or roughness. Finally, second-order models still require special treatment in regions

approaching irrotational flow. In conclusion, then, although the second-order closure models have shown a broader range of application than simple mixing-length methods, they are not universal and need further development to broaden their range of application, especially for boundary-layer flows that interact strongly with the surrounding irrotational flow.

LARGE EDDY SIMULATION OF HOMOGENEOUS TURBULENCE

The background and status of the techniques of large eddy simulation were recently reviewed by Ferziger and Leslie (Ref. 44). They gave particular attention to the methods for modelling the subgrid stresses expressed as $\langle u_i u_j \rangle$ in Eq. (14). To demonstrate the realism attained with the technique, the results of channel-flow computations were compared with data for mean-velocity profiles, U_j in Eq. (13), and mean moments, such as the pressure strain correlations. A more complete analysis of the simulation of channel flow appears in the Kim and Moin paper of this conference (Ref. 45). To supplement those papers and to demonstrate the value of turbulence simulation to statistical turbulence modelling, this author will examine what can be learned regarding statistical Reynolds stress modelling from large eddy simulations of localized flow situations.

The author is indebted to his colleague Dr. Robert Rogallo, who generously provided the results of computations he is performing on homogeneous turbulence that is experiencing decay, normal straining, or uniform shear straining. The Rogallo code has been described in Ref. 46, but has since been modified to accept uniform shearing. The code has certain unique features. The turbulence is computed in a volume of fluid that is followed in time and is defined by coordinates that move with the assigned mean velocity. In this moving frame of reference, the turbulence is spatially homogeneous. The boundary conditions on the computational volume are treated as periodic in space, which permits use of full spectral methods in the computations. The code is efficient and accurate because particular care has been exercised to conserve energy and minimize aliasing. All variables are expressed in dimensionless form and related to physical quantities (subscript e) with scaling coefficients α and β as follows:

$$\left.\begin{array}{ll} \text{Wave number or length} & k_e = \beta k \,, \quad L_e = \beta^{-1} L \\ \text{Energy} & E_e = \alpha^{-1} E \\ \text{Kinematic viscosity} & \nu_e = \alpha^{-1/2}\beta^{-1}\nu \\ \text{Time} & t_e = \alpha^{1/2}\beta^{-1} t \end{array}\right\} \qquad (50)$$

It should be noted that the kinematic viscosity is treated as constant.

In operating the Rogallo code, the turbulence is initially assigned an overall intensity with an arbitrarily assigned three-dimensional spectral distribution. In addition, the mean strain rate and kinematic viscosity are also assigned. The turbulence is then oriented in phase space randomly while conserving mass. Because of the use of random phase, the components of turbulence velocity in each direction are uncorrelated so that no shear stress exists at time = 0. In the presence of a mean shear, the shear stresses develop in a short time and the computed results become independent of the particular random phase distribution that was used to start the calculations. The initially assigned spectrum also readjusts to be consistent with the assigned strain rate and kinematic viscosity, and the instantaneous turbulence intensity.

The spectral range used in the calculations shown here has a ratio of the maximum to minimum wave number equal to 31. This ratio is established by (1) the storage capacity of the ILLIAC IV computer, which permits computations over volumes in phase space having 64 mesh points in each of three directions; and (2) the need for using two mesh spacings to define the minimum resolvable wavelength. Although this represents a very large number of computational mesh points, this spectral range is still inadequate to capture the range of wave numbers that is significant in a real turbulent flow, except for one at very small turbulence Reynolds numbers. Capturing the bulk of the significant eddy sizes and avoiding the use of a subgrid model is called an "honest" calculation. The Reynolds number appropriate to an "honest" calculation is an order of magnitude or more smaller than exists even in small scale laboratory experiments. If an "honest" calculation was to be compared with a low Reynolds number experiment, the physical output of the computations would be found from the calculations through Eqs. (50) after establishing α and β from the values of ν and E used in the calculations and the ν_e and E_e of the experiment. An alternative interpretation of these "honest" calculations is to consider ν used in the computations as an effective viscosity, which from Eqs. (13) and (14) is equivalent to the use of a constant eddy-viscosity subgrid model

$$\langle u_i' u_j' \rangle = (\nu_{eff} - \nu)(U_{i,j} + \tilde{u}_{i,j}) \qquad (51)$$

Emphasis is placed on the computation of the largest eddies in the flow, with the larger effective viscosity and a higher than real spectrum at the upper end of the wave numbers used to account for the dissipation that actually takes place at the wave numbers well beyond those in the computation. This approach presumes that the distorted spectrum at the upper end of computed wave numbers does not significantly alter the cascade of energy out of the energy-containing eddies at the low-wave-number end of the spectrum. In this approach, the scaling parameters α and β in Eqs. (5) can be established from comparing the calculated large eddy characteristics and corresponding quantities found in an experiment.

To test the validity of this alternative interpretation of Rogallo's calculations, the computed results from several cases were compared with data obtained in the experiment by Harris et al. (Ref. 47) in which a rather complete set of turbulence measurements was made in a nearly homogeneous shear flow. When the computed macroscales and turbulence kinetic energy were matched to the corresponding experimental quantities in the region where the experiment reached an asymptotic behavior, the α and β needed to utilize Eqs. (50) were established.

It was found that the best agreement between computation and experiment occurred when the effective viscosity in the computation was 15 times the molecular kinematic viscosity. A comparison of several computed

and measured statistical properties is presented in Table 1. The computations show a kinetic energy dissipation rate that is about 20% higher than the rate inferred from the measurements. This difference may not be significant however, because the energy dissipation rate is difficult to measure accurately. It is made up of direct measurements plus inferences regarding local isotropy of the small dissipative wave numbers. The excellent agreement of the mean velocity gradients indicates the large turbulence structure is properly related to the mean flow in the computation. The remaining excellent comparisons between the Reynolds stress quantities is strong evidence that the computation is capturing the larger eddy structure that is principally responsible for these quantities. This conclusion is further supported by the comparison of the computed and measured two-point correlation coefficients for u_1 in the three Cartesian directions that are shown in Fig. 16. The general character of the experimental curves in each direction is represented very well by the calculations. Some of the weaknesses of the calculations are also demonstrated in this figure. The curve of $R_{11}(r,o,o)$ is higher than that plotted from the data for the smaller separation distances. This is an indication that the smaller eddies or high-wave-number eddies in the experiment are not well represented by the computations. This was expected in a computation with limited resolution, and one in which emphasis is on accurately computing the larger eddies. In addition, it is noted that $R_{11}(r,o,o)$ has not vanished at $r_1/L_1 = 4.9$, which corresponds to 1/2 the length of each side of the computational volume. This suggests the computational volume used may have been too small and that the largest eddies could be sensitive to the periodic boundary conditions that were imposed. Even with these shortcomings, the remarkably good agreement between the experimental data and the computations encouraged the author to utilize the computations as a data base to examine some of the assumptions employed in statistical Reynolds stress modelling.

For a uniform homogeneous turbulent shear flow, the Reynolds stresses are given by

$$\frac{D\overline{u_1^2}}{Dt} = -2\overline{u_1u_2}\,U_{1,2} + 2\overline{pu_{1,1}} - 2\nu[\overline{(u_{1,1})^2} + \overline{(u_{1,2})^2} + \overline{(u_{1,3})^2}] \tag{52}$$

$$\frac{D\overline{u_2^2}}{Dt} = + 2\overline{pu_{2,2}} - 2\nu[\overline{(u_{2,1})^2} + \overline{(u_{2,2})^2} + \overline{(u_{2,3})^2}] \tag{53}$$

$$\frac{D\overline{u_3^2}}{Dt} = + 2\overline{pu_{3,3}} - 2\nu[\overline{(u_{3,1})^2} + \overline{(u_{3,2})^2} + \overline{(u_{3,3})^2}] \tag{54}$$

and

$$\frac{D\overline{u_1u_2}}{Dt} = -\overline{u_1u_2}\,U_{1,2} + \overline{p(u_{1,2} + u_{2,1})} - 2\nu[\overline{u_{1,1}u_{2,1}} + \overline{u_{1,2}u_{2,2}} + \overline{u_{1,3}u_{2,3}}] \tag{55}$$

Closure of these equations requires expressing the correlation of pressure and rate of strain and the dissipation terms containing ν in terms of the Reynolds stresses, themselves, and the mean flow. The pressure rate-of-strain model to be evaluated here is represented by Eqs. (36) and (37). The dissipation terms in Eqs. (51) through (54) are usually replaced by the symbols ε_{11}, ε_{22}, ε_{33}, and ε_{12}. In terms of these quantities, the dissipation of the turbulence kinetic energy is given by

$$\varepsilon = \frac{1}{2}(\varepsilon_{11} + \varepsilon_{22} + \varepsilon_{33}) \tag{56}$$

It is usually assumed in modelling that the dissipation takes place at the smallest eddies and is, therefore, an isotropic phenomenon represented mathematically as

$$\varepsilon_{ij} = \frac{2}{3}\varepsilon\delta_{ij} \tag{57}$$

To learn if the computations are consistent with the assumption of isotropic dissipation in a shear flow, the computed values of ε_{ij} corresponding to each Reynolds stress are plotted against a measure of the anisotropy, $u_iu_j/e - 2/3\,\delta_{ij}$, in Fig 17. The values corresponding to the different Reynolds stresses for a range of turbulence Reynolds numbers generally lie along a straight line with a slope of about 0.7. If the dissipation had been isotropic, in the coordinates of the figure, these points would have been located on the axis or at an ordinate equal to zero. The computations show the dissipation to be <u>anisotropic</u> and require that Eq. (57) be modified to

$$\varepsilon_{ij} = \frac{2}{3}\varepsilon\delta_{ij} + 0.7\,\frac{\overline{u_iu_j}}{e} - \frac{2}{3}\delta_{ij} \tag{58}$$

for the shear flow. What is normally termed dissipation in a large eddy simulation actually represents the component energies that are cascaded toward the high wave number end of the calculation to be then drained from the calculation by the subgrid model. It is no surprise then that the cascade process reflects the anisotropy of the larger eddies. The emphasis on the behavior of the large eddies possibly is an advantage: it may be just what is required in Reynolds stress modelling, which also addresses the behavior of the larger eddies.

Figure 18 shows the components of dissipation as functions of anisotropy for the case of a turbulent flow relaxing after it had been instantaneously distorted with normal strains in the x_2 and x_3 directions. In this case, the computed results generally lie along the coordinate axis and the dissipation is approximately isotropic even though the flow itself is still anisotropic.

The homogeneous flow relaxing after instantaneous distortion by normal strains is also an excellent case for examining the first term in the pressure rate of strain relationship represented by Eq. (36). The terms in Eq. (36) preceded by $\hat{\alpha}$, $\hat{\beta}$, and $\hat{\gamma}$ are identically zero in the absence of continuing mean strain. The C_1 were evaluated from the computed turbulence moments for a case distorted in all three directions. It was found that C_1 was reasonably insensitive to the direction of the component considered. The C_1 (based on U^2) is plotted as a function of the turbulence Reynolds number $e^2/\varepsilon\nu_{eff}$ in Fig. 19. The numbers adjacent to the symbols represent the magnitude of the largest anisotropy in the three components. Three

different values of ν_{eff} were used in the calculations to extend the range of the turbulent Reynolds number. It is observed that if the largest component of anisotropy is less than 0.25, that is, if

$$\frac{u_2^2}{e} - \frac{2}{3}\delta_{ij} < 0.25 \tag{59}$$

the values of C_1 collapse onto a single curve. For those values of isotropy where the points depart from a single curve, the linear form of the Rotta term expressed in anisotropy can be considered to have failed. It is also noted that for values of anisotropy satisfying (59), the so-called "constant" C_1 still has a strong Reynolds number dependence.

The value of C_1 was also evaluated from the homogeneous shear flow computation of the pressure rate-of-strain correlation and Eqs. (36) and (37). To do this most simply, the interrelationships between $\hat{\alpha}$, $\hat{\beta}$, and $\hat{\gamma}$ derived by Launder et al. (Ref. 14) following Rotta's suggestion (Ref. 8) were utilized. The C_1 formed from these computations is plotted as a function of turbulence Reynolds number in Fig. 20. Again, the maximum anisotropy is indicated at the plotted points. For comparison, the C_1 from the normally strained flow, with the value of maximum anisotropy characteristic of shear flow, are also plotted on the figure. Shearing the flow tends to increase the turbulence Reynolds number so that the regions of the two flows do not overlap. The same magnitude of anisotropy is used for both flows to account for a similar departure from the linear Rotta form in each. It is observed that the line segments associated with the different types of flow fields do not appear to form a common curve. This would imply that the pressure rate-of-strain model represented by Eqs. (36) and (37) is not as universal as is suggested by its tensor form. It is most interesting, however, to note that if the C_1 is considered to be the coefficient of the sum of the pressure rate-of-strain correlation and the anisotropic dissipation, the dashed curves on Fig. 20, the two flow fields tend to produce a common curve. It appears that only the sum of the dissipation and pressure rate-of-strain can be modelled universally. This observation is consistent with the theoretical approach adopted by Lumley and Newman (Ref. 48). It should be noted, again, that the anisotropy on the figure is outside the region of applicability of the Rotta relationship and that shear flows with lesser anisotropy would require larger values of C_1 for the pressure rate of strain contribution.

The values of C_1, $\hat{\alpha}$, $\hat{\beta}$, and $\hat{\gamma}$ that conform to the high end of the turbulence Reynolds number in these calculations are shown in Table 2 along with those used in the Launder et al. (Ref. 14) model and the RSE model described here. The agreement between the computations of Launder et al. and those of Rogallo is excellent and is primarily due to the ability of the computations to yield good values of the Reynolds stresses in equilibrium shear flow (Table 1). The requirement of $\hat{\alpha} = \hat{\beta}$ in the RSE model apparently requires considerable compensation in all the other terms to result in the proper Reynolds stress ratios for uniform shear flows.

Concluding Remarks Regarding Large Eddy Simulations

Although this demonstration of the use of large-eddy simulations for guiding Reynolds stress modelling has been limited to homogeneous flows, its utility as a research tool shows great promise. Although the procedure is quite costly in terms of computer time (the calculations shown here require about 1.5 hr ILLIAC IV time per test case), the potential gains in computer technology (Ref. 1) should make large eddy simulations a research tool that will be available to most research laboratories in a decade or so. It is this author's belief that research activities involving coordinated theory, experimentation, and computer simulations will in the reasonably near future not only bring about a much clearer understanding of the physics of turbulence, but may even permit the development of predictive engineering methods for flow fields of technological interest.

REFERENCES

1. Chapman, D. R.: Computational Aerodynamics Development and Outlook. AIAA Dryden Lectureship in Research, AIAA Paper 79-0129, Jan. 15-17, 1979.

2. Leonard, A.: On the Energy Cascade in Large-Eddy Simulations of Turbulent Fluid Flows. Adv. in Geophysics, vol. 18A, 1974, p. 237.

3. Kline, S. J., Morkovin, M. V., Sovran, G., and Cockrell, D. J.: Proc. Computation of Turbulent Boundary Layers, vol. 1, Methods, Predictions, Evaluation and Flow Structure, 1968 AFOSR-IFP-Stanford Conference, Stanford U., Stanford, Calif., Aug. 18-25, 1968.

4. Cebeci, T. and Smith, A. M. O.: Analysis of Turbulent Boundary Layers. Academic Press, New York, 1974.

5. Kays, W. M.: Heat Transfer to the Transpired Turbulent Boundary Layer. Report No. HMT-14, Thermosciences Division, Dept. of Mechanical Engineering, Stanford U., Stanford Calif., June 1971.

6. Kolmogorov, A. N.: Equations of a Turbulent Motion of an Incompressible Fluid. Izv. Akad. Nauk, SSR Ser. fiz. VI, no. 1-2, 1942, pp. 56-58.

7. Chou, P. Y.: On Velocity Correlations and the Solutions of the Equations of Turbulent Fluctuation. Quart. Appl. Math, vol. 3, no. 1, 1945.

8. Rotta, J.: Statistische Theorie nicht-homogener Turbulenz, 1. Mitteilung, Zeitschrift Fuer Physik, vol. 129, 1951, pp. 547-572.

9. Rotta, J.: Statistische Theorie nicht-homogener Turbulenz, 2 Mitteilung, Zeitschrift fuer Physik, vol. 131, 1951, pp. 51-77.

10. Wilcox, D. C. and Traci, R. M.: A Complete Model of Turbulence. AIAA Paper 76-351, July 1976.

11. Wilcox, D. C. and Rubesin, M. W.: Progress in Turbulence Modeling for Complex Flow Fields, Including Effects of Compressibility. NASA TP-1517, 1979.

12. Saffman, P. G.: A Model for Inhomogeneous Turbulent Flow. Proc. Roy. Soc. Lond. A 317, 1970, pp. 417-433.

13. Jones, W. P. and Launder, B. E.: The Prediction of Laminarization with the Two-Equation Model of Turbulence. Int. J. Heat Mass Transf., vol. 15, 1972, pp. 301-314.

14. Launder, B. E., Reece, G. J., and Rodi, W.: Progress in the Development of a Reynolds Stress Turbulence Closure. J. Fluid Mech., vol. 68, pt. 3, 1975, pp. 537-566.

15. Rubesin, M. W., Crisalli, A. J., Lanfranco, M. J., and Acharya, M.: A Critical Evaluation of Invariant Second-Order Closure Models for Subsonic Boundary Layers. Proc. Symposium on Turbulent Shear Flows, University Park, Penn., Apr. 18-20, 1977, pp. 4.1-4.38.

16. Favre, A.: Equations des Gaz Turbulents Compressibles. J. Mecan., vol. 4, no. 3, Sept. 1965, pp. 361-390.

17. Escudier, M. P.: The Distribution of the Mixing Length in Turbulent Flows Near Walls. Rept. TWF/TN/1, Imperial College, London, 1965.

18. Saffman, P. G.: Development of a Complete Model for the Calculation of Turbulent Shear Flows. Paper presented at meeting on "Turbulence and Dynamical Systems." Duke U., Durham, N.C., Apr. 1976.

19. Tucker, H. J. and Reynolds, A. J.: The Distortion of Turbulence by Irrotational Plane Strain. J. Fluid Mech. JFM, vol. 32, pt. 4, 1968, pp. 657-673.

20. Ibbetson, A. and Tritton, D. J.: Experiments on Turbulence in Rotating Fluid. J. Fluid Mech., vol. 68, pt. 4, 1975, pp. 639-672.

21. Bradshaw, P.: The Response of a Constant-Pressure Turbulent Boundary Layer to the Sudden Application of an Adverse Pressure Gradient. ARC R&M 3575, 1969.

22. Coles, D. E. and Hirst, E. A.: Proc. Computation of Turbulent Boundary Layers, vol. II, Compiled Data, 1968 AFOSR-IFP-Stanford Conference, Stanford U., Stanford, California, Aug. 18-25, 1968.

23. Rao, G. N. V.: The Law of the Wall in a Thick Axisymmetric Turbulent Boundary Layer. J. Appl. Mech., vol. 89, 1967, pp. 237-238.

24. Richmond, R.: Experimental Investigation of Thick Axisymmetric Boundary Layer on Cylinders in Subsonic and Hypersonic Speeds. Ph.D. Thesis, California Institute of Technology, Pasadena, Calif., 1957.

25. Lohmann, R. P.: The Response of a Developed Turbulent Boundary Layer to Local Transverse Surface Motion. Trans. ASME, J. Fluids Eng., Sept. 1976, pp. 354-363. (Also Ph.D. Thesis, University of Connecticut, Storrs, Conn., 1974.)

26. Bissonnette, L. R. and Mellor, G. L.: Experiments on the Behavior of an Axisymmetric Turbulent Boundary Layer with a Sudden Circumferential Strain. J. Fluid Mech., vol. 63, pt. 2, Apr. 1974, pp. 369-413. (Also Ph.D. Thesis by Bissonnette, L. R., Princeton University, Princeton, N.J., 1970.)

27. Willmarth, W. W., Winkel, R. E., Bogar, T. J., and Sharma, L. K.: Axially Symmetric Turbulent Boundary Layers on Cylinders: Mean Velocity Profiles and Wall Pressure Fluctuations. University of Michigan, Department of Aerospace Engineering Report 021490-3-7, June, 1975.

28. Bradshaw, P.: Effects of Streamline Curvature on Turbulent Flow. AGARD-AG-169, Aug. 1973.

29. So, R. M. C. and Mellor, G. L.: An Experimental Investigation of Turbulent Boundary Layers Along Curved Surfaces. NASA CR-1940, 1972.

30. Wilcox, D. C. and Alber, I. E.: A Turbulence Model for High-Speed Flows, Proc. 1972 Heat Transfer and Fluid Mechanics Institute, Stanford U. Press, 1972, pp. 231-252.

31. Rubesin, M. W.: A One-Equation Model of Turbulence for Use with the Compressible Navier-Stokes Equations. NASA TM X-73,128, 1976.

32. Coakely, T. J., Viegas, J. R., and Horstman, C. C.: Evaluation of Turbulence Models for Three Primary Types of Shock Separated Boundary Layers. AIAA Paper 77-672, June 1977.

33. Hopkins, E. J. and Inouye, M.: An Evaluation of Theories for Prediction of Turbulent Skin Friction and Heat Transfer on Flat Plates at Supersonic and Hypersonic Mach Numbers. AIAA J., vol. 9, no. 6, 1971, pp. 993-1003.

34. Lewis, J. E., Gran, R. L., and Kubota, T.: An Experiment on the Adiabatic Compressible Turbulent Boundary Layer in Adverse and Favorable Pressure-Gradients. J. Fluid Mech., vol. 51, pt. 4, 1972, pp. 657-672.

35. Marvin, J. G. and Sheaffer, Y. S.: A Method for Solving the Nonsimilar Boundary-Layer Equations Including Foreign Gas Injection. NASA TN D-5516, 1969.

36. Horstman, C. C., Kussoy, M. I., and Lanfranco, M. J.: An Evaluation of Several Compressible Turbulent Boundary Layer Models: Effect of Pressure Gradient and Reynolds Number. AIAA Paper 78-1160, July 10-12, 1978.

37. Sullivan, R. D.: GYC: A Program to Compute the Turbulent Boundary Layer on a Rotating Cone. A.R.A.P. Working Paper 76-2, Aug. 1976.

38. Mateer, G. G. and Viegas, J. R.: Effect of Mach and Reynolds Numbers on a Normal Shock Wave/Turbulent Boundary Layer Interaction. AIAA Paper 79-1502, July 23-25, 1979.

39. Settles, G. S., Vas, I. E., and Bogdonoff, S. M.: Details of a Shock-Separated Turbulent Boundary Layer at a Compression Corner. AIAA J., vol. 14, 1976, pp. 1709-1715.

40. Viegas, J. R. and Horstman, C. C.: Comparison of Multiequation Turbulence Models for Several Shock Separated Boundary Layer Flows. AIAA Paper 78-1165, July 10-12, 1978.

41. Viswanath, P. R., Cleary, J. W., Seegmiller, H. L., and Horstman, C. C.: Trailing-Edge Flows at High Reynolds Number. AIAA Paper 79-1503, July 23-25, 1979.

42. Aguilar, R.: A Numerical Analysis of Turbulent Flow Along an Abruptly Rotated Cylinder. Ph.D. Thesis, Virginia Polytechnic Inst. and State U., Blacksburg, Va., 1976.

43. Higuchi, H. and Rubesin, M. W.: Behavior of a Turbulent Boundary Layer Subjected to Sudden Transverse Strain. AIAA Paper 78-201, Jan. 16-18, 1978.

44. Ferziger, J. H. and Leslie, D. C.: Large Eddy Simulation: A Predictive Approach to Turbulent Flow Computation. AIAA Paper 79-1471, July 23-25, 1979.

45. Kim, John and Moin, Parviz: Large Eddy Simulation of Turbulent Channel Flow. Paper presented at AGARD Symposium Turbulent Boundary Layer — Experiment Theory and Modelling, 24-27 Sept. 1979, at The Hague, Netherlands.

46. Rogallo, Robert S.: An ILLIAC Program for the Numerical Simulation of Homogeneous Incompressible Turbulence. NASA TM-73,203, 1977.

47. Harris, V. G., Graham, J. A. H., and Corrsin, S.: Further Experiments in Nearly Homogeneous Turbulent Shear Flow. J. Fluid Mech., vol. 81, pt. 4, 1977, pp. 657-687.

48. Lumley, J. L. and Newman, G. R.: The Return to Isotropy of Homogeneous Turbulence. J. Fluid Mech., vol. 82, pt. 1, 1977, pp. 161-178.

TABLE 1. COMPARISON OF ROGALLO'S SHEAR FLOW CALCULATIONS WITH THE EXPERIMENTAL DATA OF HARRIS, GRAHAM, AND CORRSIN[a]

Quantity	Experiment	Computation
Dissipation rate, $cm^2\ sec^{-3}$	3.28E+04	3.92E+04
Mean-velocity gradient, $U_{1,2}\ sec^{-1}$	44.0	45.3
Angle of principal stresses, deg	-22.3	-22.6
Ratio of principal stresses	4.06	5.24
u_1u_1/e	1.00	1.01
u_2u_2/e	0.40	0.36
u_3u_3/e	0.60	0.63
$-u_1u_2/e$	0.30	0.33

[a]Scaling established by matching turbulence kinetic energy and streamwise macroscales. Turbulence model $\nu_{eff}/\nu = 15$.

TABLE 2. PRESSURE RATE OF STRAIN CORRELATION MODELLING COEFFICIENTS

	Launder, Reece, and Rodi model	Wilcox and Rubesin model	Rogallo's computations
C_1	1.5[a]	4.5[a]	1.5[a]
$\hat{\alpha}$	0.76	0.5	0.78
$\hat{\beta}$	0.11	0.5	0.23
$\hat{\gamma}$	0.36	1.33	0.55

[a]Includes effects of anisotropic dissipation.

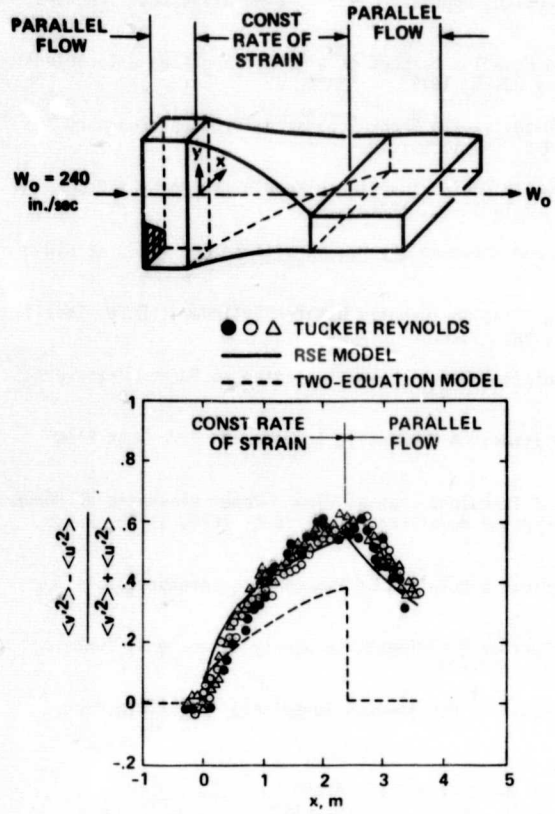

Fig. 1. Comparison of computed and measured distortion parameter for the Tucker-Reynolds plane strain flow.

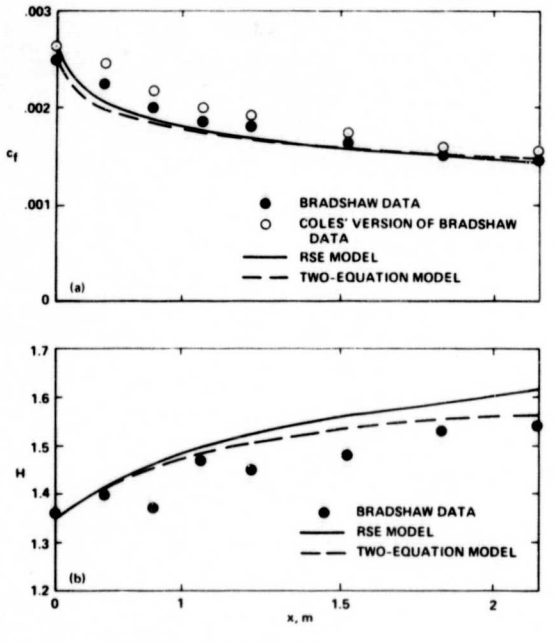

(a) Skin-friction distribution.
(b) Shape-factor distribution.

Fig. 2. Comparison of computed and measured skin friction and shape factor for the Bradshaw adverse-pressure-gradient flow.

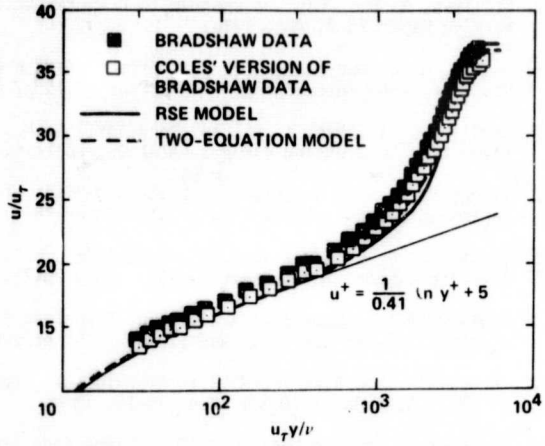

Fig. 3. Comparison of computed and measured velocity profiles for the Bradshaw adverse-pressure-gradient flow; x = 2.1 m.

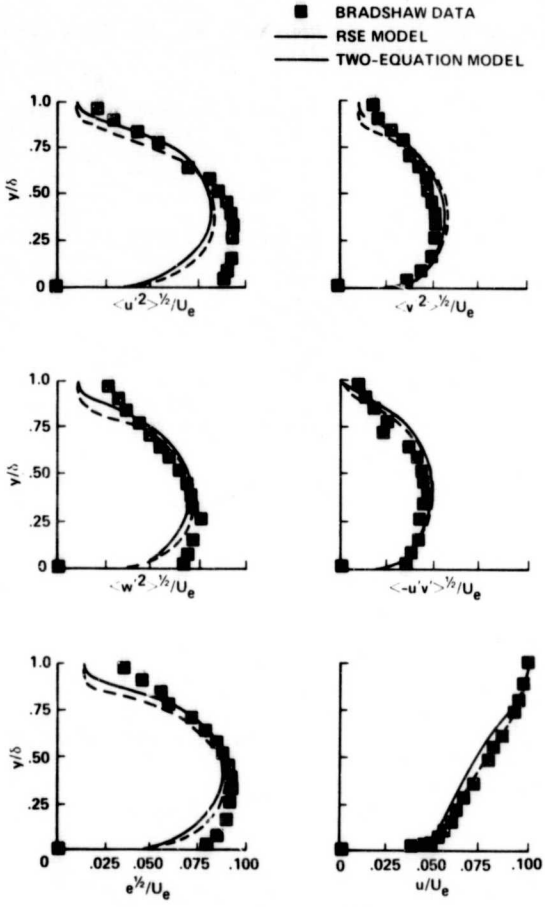

Fig. 4. Mean field profiles for the Bradshaw adverse-pressure gradient flow; x = 2.1 m.

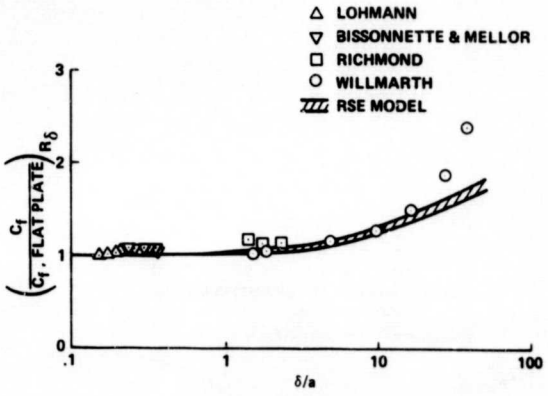

Fig. 5. Effect of transverse surface curvature on skin friction.

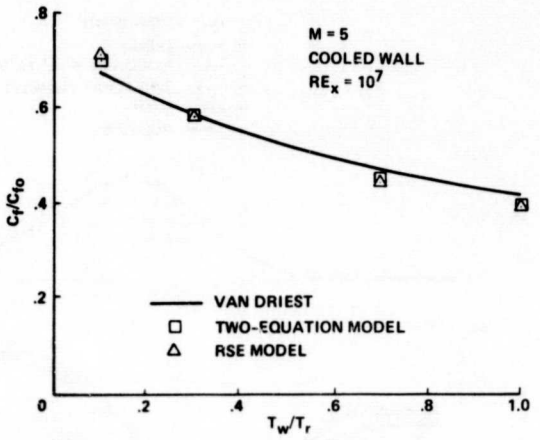

Fig. 7. Effect of surface cooling on the skin friction on a flat plate.

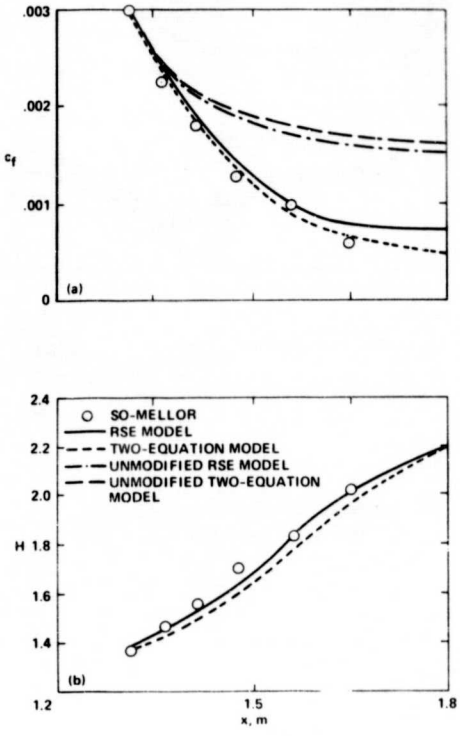

(a) Skin-friction distribution.
(b) Shape-factor distribution.

Fig. 6. Comparison of computed and measured skin friction and shape factor for flow over a convex wall with adverse pressure gradient.

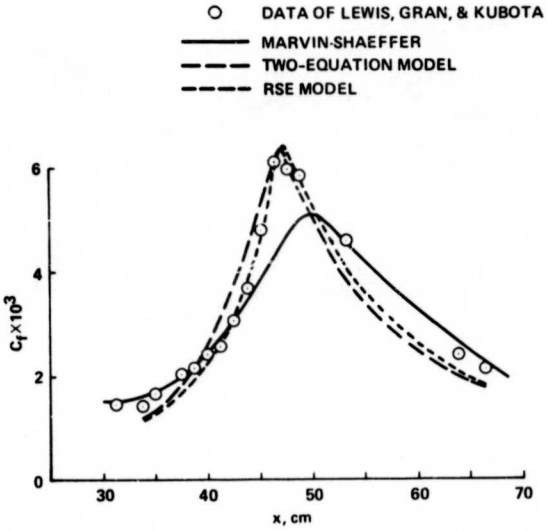

Fig. 8. Skin-friction coefficient distribution in a region of large pressure gradient at $M_\infty = 4$.

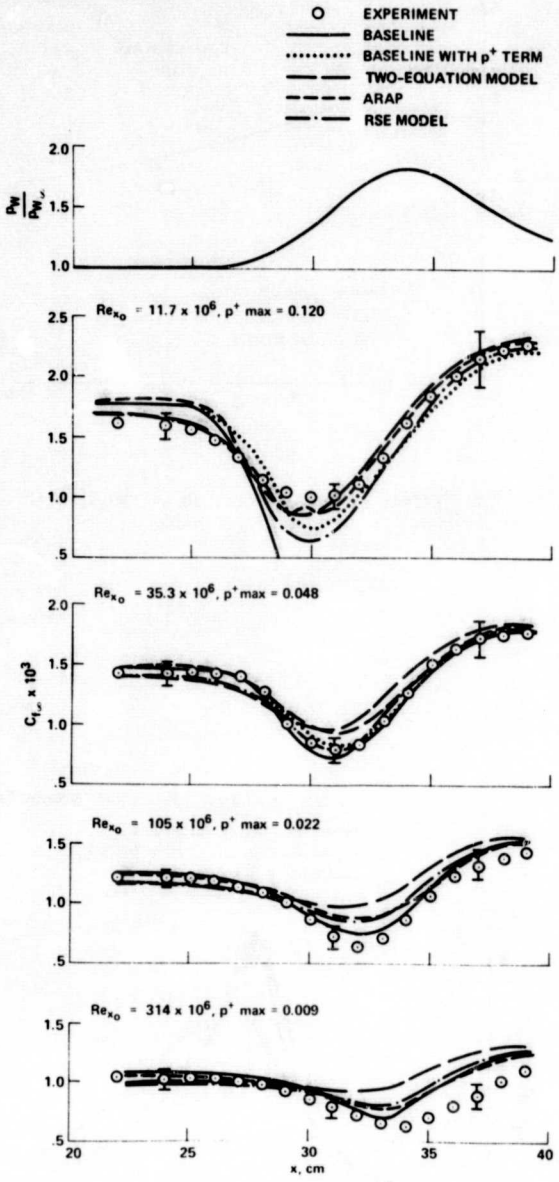

Fig. 9. Skin-friction distribution in region of large pressure gradients at high Reynolds numbers, $M_\infty = 2.3$.

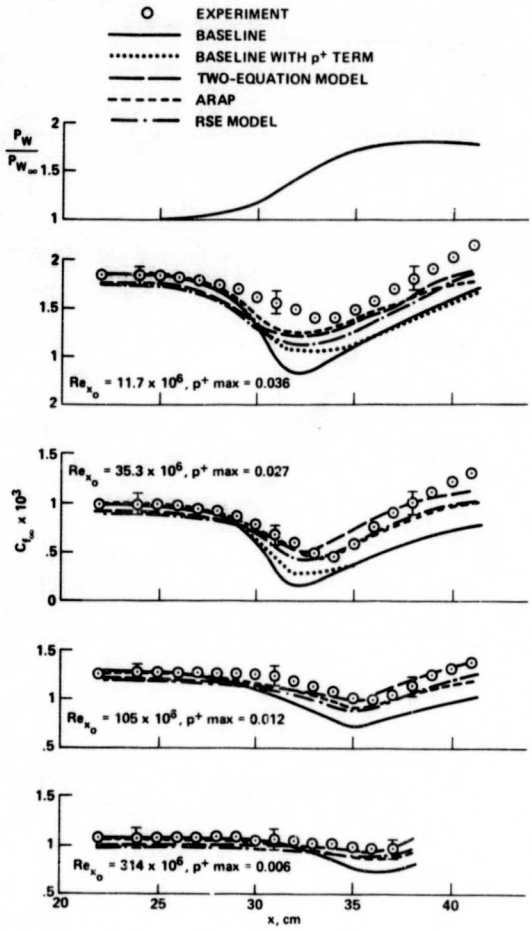

Fig. 10. Skin-friction distribution in extended region of large pressure gradient at high Reynolds numbers, $M_\infty = 2.3$.

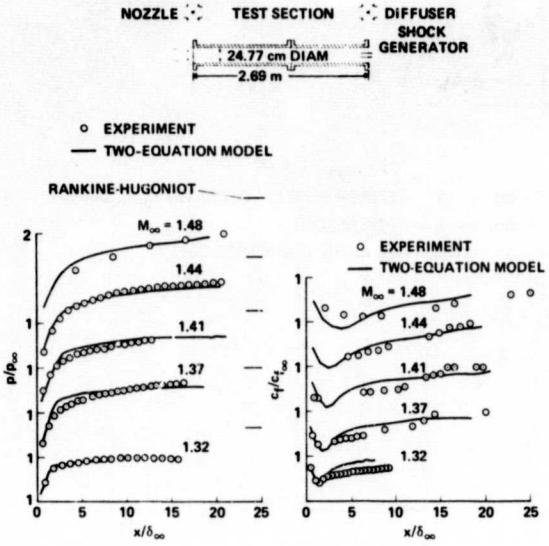

Fig. 11. Comparison of computations and surface measurements of pressure and skin friction in region of shock wave, boundary-layer interaction at low supersonic speeds.

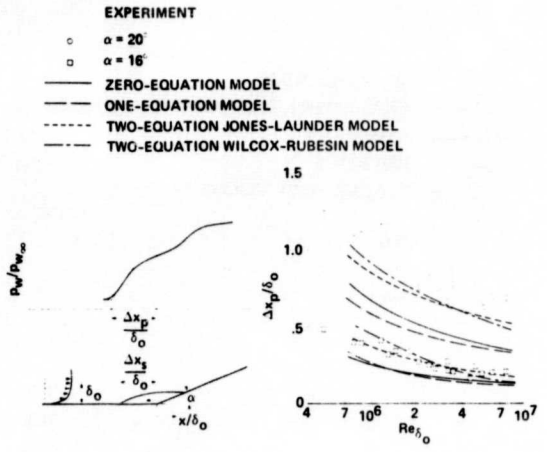

Fig. 13. Comparison of computations and measurements of the effect of Reynolds number on the extent of upstream pressure influence of a supersonic compression corner, M = 2.8.

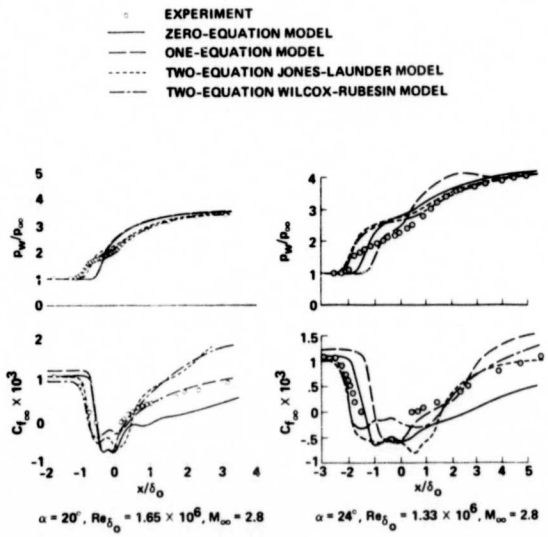

Fig. 12. Comparison of computations and surface measurements of pressure and skin friction in the region of a compression corner at supersonic speeds.

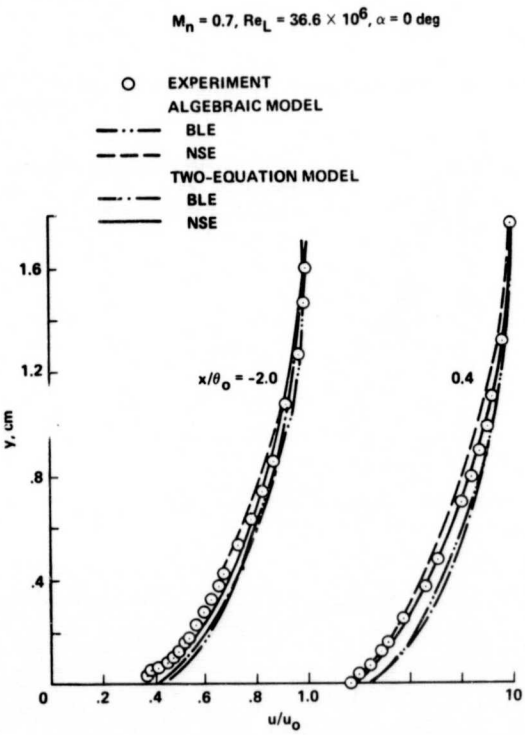

Fig. 14. Comparison of computed and measured mean-velocity profiles upstream and downstream of sharp trailing edge with a 12.5° wedge angle.

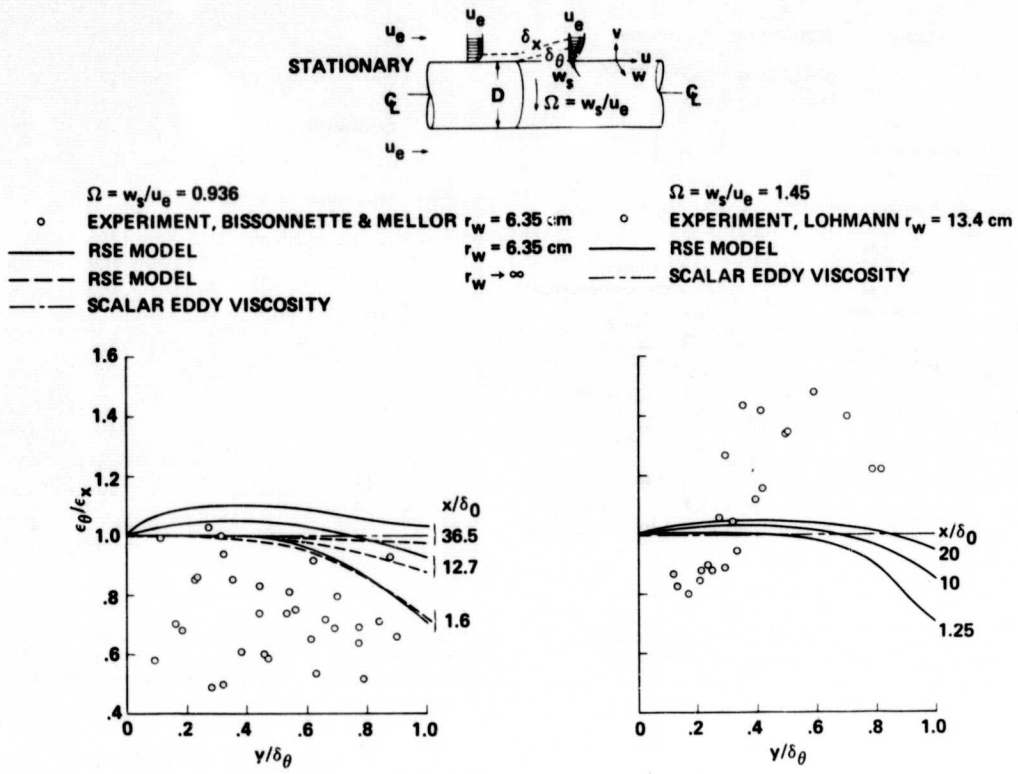

Fig. 15. Ratio of the transverse and longitudinal eddy viscosities in the region of a sudden application of transverse shear.

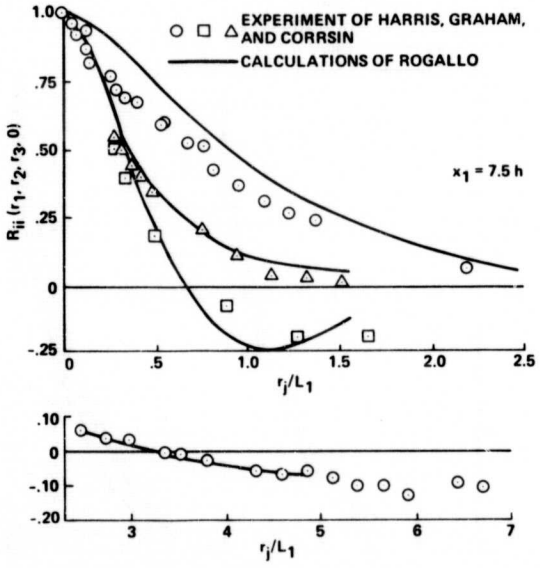

Fig. 16. Two-point correlation coefficients of u_1 along the three Cartesian axes.

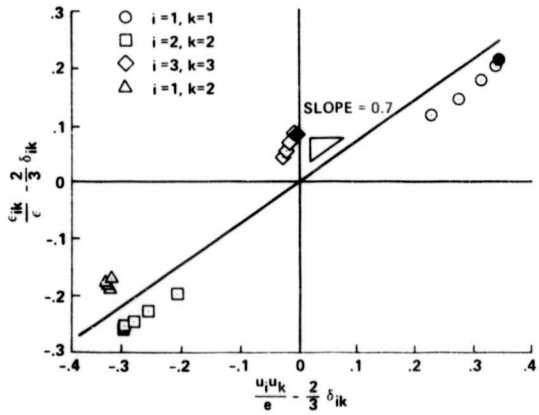

Fig. 17. Components of dissipation within a homogeneous shear flow.

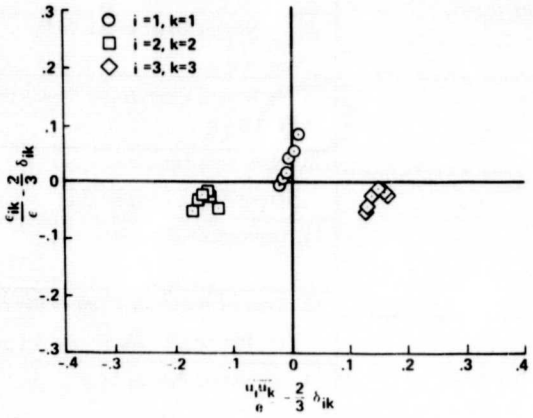

Fig. 18. Components of didsipation in a relaxing homogeneous turbulence after sudden normal distortion.

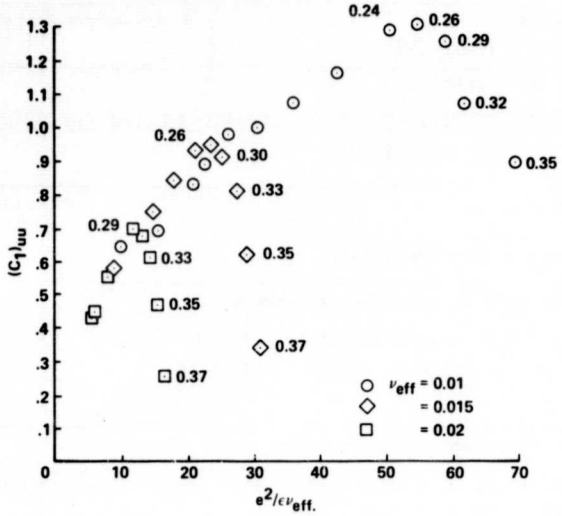

Fig. 19. Behavior of the coefficient in the Rotta pressure rate of strain correlation term in a relaxing homogeneous flow after sudden distortion by normal forces. Numbers near symbols represent the value of the largest component of anisotropy present.

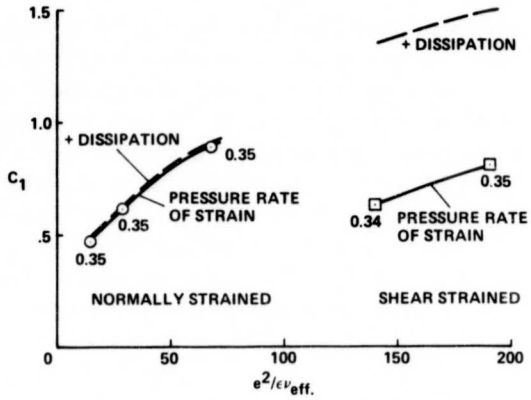

Fig. 20. Reconciliation of modeling the Rotta term in normally and shear strained flows. Numbers near the symbols represent the value of the largest component of anisotropy present.